Low-loss asymptotically single-mode propagation in large-core OmniGuide fibers

Steven G. Johnson, Mihai Ibanescu, M. Skorobogatiy,
Ori Weisberg, Torkel D. Engeness, Marin Soljačić,
Steven A. Jacobs, J. D. Joannopoulos, and Yoel Fink

*OmniGuide Communications, One Kendall Square, Building 100 #3,
Cambridge MA 02139*

maksim@omni-guide.com

Abstract: We present the light-propagation characteristics of OmniGuide fibers, which guide light by concentric multi-layer dielectric mirrors having the property of omnidirectional reflection. We show how the lowest-loss TE_{01} mode can propagate in a single-mode fashion through even large-core fibers, with other modes eliminated asymptotically by their higher losses and poor coupling, analogous to hollow metallic microwave waveguides. Dispersion, radiation leakage, material absorption, nonlinearities, bending, acircularity, and interface roughness are considered with the help of leaky modes and perturbation theory, and both numerical results and general scaling relations are presented. We show that cladding properties such as absorption and nonlinearity are suppressed by many orders of magnitude due to the strong confinement in a hollow core, and other imperfections are tolerable, promising that the properties of silica fibers may be surpassed even when nominally poor materials are employed.

© 2001 Optical Society of America

OCIS codes: (060.2310) Fiber optics; (230.1480) Bragg reflectors

References and links

1. J. D. Joannopoulos, R. D. Meade, and J. N. Winn, *Photonic Crystals: Molding the Flow of Light* (Princeton, 1995).
2. R. F. Cregan, B. J. Mangan, J. C. Knight, T. A. Birks, P. S.-J. Russell, and P. J. Roberts, "Single-mode photonic band gap guidance of light in air," Science **285,** 1537–1539 (1999).
3. P. Yeh, A. Yariv, and E. Marom, "Theory of Bragg fiber," J. Opt. Soc. Am. **68,** 1196–1201 (1978).
4. N. J. Doran and K. J. Bulow, "Cylindrical Bragg fibers: a design and feasibility study for optical communications," J. Lightwave Tech. **1,** 588–590 (1983).
5. A. N. Lazarchik, "Bragg fiber lightguides," Radiotekhnika i electronika **1,** 36–43 (1988).
6. C. M. de Sterke and I. M. Bassett, "Differential losses in Bragg fibers," J. Appl. Phys. **76,** 680–688 (1994).
7. Y. Fink, D. J. Ripin, S. Fan, C. Chen, J. D. Joannopoulos, and E. L. Thomas, "Guiding optical light in air using an all-dielectric structure," J. Lightwave Tech. **17,** 2039–2041 (1999).
8. F. Brechet, P. Roy, J. Marcou, and D. Pagnoux, "Singlemode propagation into depressed-core-index photonic-bandgap fibre designed for zero-dispersion propagation at short wavelengths," Elec. Lett. **36,** 514–515 (2000).
9. F. Brechet, P. Leproux, P. Roy, J. Marcou, and D. Pagnoux, "Analysis of bandpass filtering behavior of singlemode depressed-core-index photonic bandgap fibre," Elec. Lett. **36,** 870–872 (2000).
10. M. Ibanescu, Y. Fink, S. Fan, E. L. Thomas, and J. D. Joannopoulos, "An all-dielectric coaxial waveguide," Science **289,** 415–419 (2000).
11. Y. Xu, R. K. Lee, and A. Yariv, "Asymptotic analysis of Bragg fibers," Opt. Lett. **25,** 1756–1758 (2000).
12. T. Kawanishi and M. Izutsu, "Coaxial periodic optical waveguide," Opt. Express **7,** 10–22 (2000), http://www.opticsexpress.org/oearchive/source/22933.htm.

13. Y. Xu and A. Yariv, "Asymptotic analysis of Bragg fibers and dielectric coaxial fibers," In *Proc. SPIE*, A. Dutta, A. A. S. Awwal, N. K. Dutta, and K. Okamoto, eds.,**4532,** 191–205 (2001).

14. Y. Fink, J. N. Winn, S. Fan, C. Chen, J. Michel, J. D. Joannopoulos, and E. L. Thomas, "A dielectric omnidirectional reflector," Science **282,** 1679–1682 (1998).

15. R. Ramaswami and K. N. Sivarajan, *Optical Networks: A Practical Perspective* (Academic Press, London, London, 1998).

16. E. A. Marcatili and R. A. Schmeltzer, "Hollow metallic and dielectric waveguides for long distance optical transmission and lasers," Bell Syst. Tech. J. **43,** 1783–1809 (1964).

17. W. D. Warters, "WT4 millimeter waveguide system: introduction," Bell Syst. Tech. J. **56,** 1825–1827 (1977), the introduction to a special issue with many useful articles.

18. M. Miyagi, A. Hongo, and S. Kawakami, "Transmission characteristics of dielectric-coated metallic waveguides for infrared transmission: slab waveguide model," IEEE J. Quantum Elec. **QE-19,** 136–145 (1983).

19. M. Miyagi and S. Kawakami, "Design theory of dielectric-coated circular metallic waveguides for infrared transmission," J. Lightwave Tech. **2,** 116–126 (1984).

20. J. A. Harrington, "A review of IR transmitting, hollow waveguides," Fiber Integr. Opt. **19,** 211–227 (2000).

21. M. Ibanescu *et al.*, to be published in 2002.

22. P. Yeh, *Optical Waves in Layered Media* (Wiley, New York, 1988).

23. A. W. Snyder and J. D. Love, *Optical Waveguide Theory* (Chapman and Hall, London, 1983).

24. S. A. Jacobs *et al.*, to be published in 2002.

25. L. Grüner-Nielsen, S. N. Knudsen, B. Edvold, T. Veng, D. Magnussen, C. C. Larsen, and H. Damsgaard, "Dispersion compensating fibers," Optical Fiber Tech. **6,** 164–180 (2000).

26. W. H. Weber, S. L. McCarthy, and G. W. Ford, "Perturbation theory applied to gain or loss in an optical waveguide," Appl. Opt. **13,** 715–716 (1974).

27. A. Kumar, S. I. Hosain, and A. K. Ghatak, "Propagation characteristics of weakly guiding lossy fibers: an exact and perturbation analysis," Optica Acta **28,** 559–566 (1981).

28. Z. Pantic and R. Mittra, "Quasi-TEM analysis of microwave transmission lines by the finite-element method," IEEE Trans. Microwave Theory Tech. **MTT-34,** 1096–1103 (1986).

29. S. X. She, "Propagation loss in metal-clad waveguides and weakly absorptive waveguides by a perturbation method," Opt. Lett. **15,** 900–902 (1990).

30. V. L. Gupta and E. K. Sharma, "Metal-clad and absorptive multilayer waveguides: an accurate perturbation analysis," J. Opt. Soc. Am. A **9,** 953–956 (1992).

31. C. Themistos, B. M. A. Rahman, A. Hadjicharalambous, and K. T. V. Grattan, "Loss/gain characterization of optical waveguides," J. Lightwave Tech. **13,** 1760–1765 (1995).

32. D. Sarid and G. I. Stegeman, "Optimization of the effects of power dependent refractive indices in optical waveguides," J. Appl. Phys. **52,** 5439–5441 (1981).

33. V. P. Tzolov, M. Fontaine, N. Godbout, and S. Lacroix, "Nonlinear self-phase-modulation effects: a vectorial first-order perturbation approach," Opt. Lett. **20,** 456–458 (1995).

34. R. S. Grant, "Effective non-linear coefficients in optical waveguides," Optical and Quantum Elec. **28,** 1161–1173 (1996).

35. B. Z. Katsenelenbaum, L. Mercader del Río, M. Pereyaslavets, M. Sorolla Ayza, and M. Thumm, *Theory of Nonuniform Waveguides: The Cross-Section Method* (Inst. of Electrical Engineers, London, 1998).

36. L. Lewin, D. C. Chang, and F. Kuester, *Electromagnetic Waves and Curved Structures* (P. Peregrinus, England, 1977).

37. M. Miyagi, K. Harada, and S. Kawakami, "Wave propagation and attenuation in the general class of circular hollow waveguides with uniform curvature," IEEE Trans. Microwave Theory Tech. **MTT-32,** 513–521 (1984).

38. J. D. Jackson, *Classical Electrodynamics*, 3rd ed. (Wiley, New York, 1998).

39. M. Lohmeyer, N. Bahlmann, and P. Hertel, "Geometry tolerance estimation for rectangular dielectric waveguide devices by means of perturbation theory," Opt. Commun. **163,** 86–94 (1999).

40. D. Q. Chowdhury and D. A. Nolan, "Perturbation model for computing optical fiber birefringence from a two-dimensional refractive-index profile," Opt. Lett. **20,** 1973–1975 (1995).

41. D. Q. Chowdhury, "Comparison between optical fiber birefringence induced by stress anisotropy and geometric deformation," IEEE J. Selected Topics Quantum Elec. **6,** 227–232 (2000).

42. V. P. Kalosha and A. P. Khapalyuk, "Mode birefringence in a single-mode elliptic optical fiber," Sov. J. Quantum Elec. **13,** 109–111 (1983).

43. V. P. Kalosha and A. P. Khapalyuk, "Mode birefringence of a three-layer elliptic single-mode fiber waveguide," Sov. J. Quantum Elec. **14,** 427–430 (1984).

44. M. Skorobogatiy *et al.*, to be published in 2002.

45. D. Marcuse, *Theory of Dielectric Optical Waveguides* (Academic, New York, 1974).

46. *Characteristics of a single-mode optical fibre cable* (Intl. Telecom. Union, 2000), No. G.652.

47. A. W. Snyder, "Radiation losses due to variations of radius on dielectric or optical fibers," IEEE

Trans. Microwave Theory Tech. **MTT-18,** 608–615 (1970).

48. S. G. Johnson *et al.*, to be published in 2002.

49. C. Cohen-Tannoudji, B. Din, and F. Laloë, *Quantum Mechanics* (Hermann, Paris, 1977), *Vol. One*, ch. 2; and *Vol. Two*, ch. 11 and 13.

50. L. A. Yudin, S. P. Efimov, M. I. Kapchinsky, and I. L. Korenev, "Electrodynamics as a problem of eigenvalues," Phys. Plasmas **3,** 42–58 (1996).

51. N. W. Ashcroft and N. D. Mermin, *Solid State Physics* (Holt Saunders, Philadelphia, 1976).

52. A. Messiah, *Quantum Mechanics: Vol. II* (Wiley, New York, 1976), ch. 17.

53. G. H. Song and W. J. Tomlinson, "Fourier analysis and synthesis of adiabatic tapers in integrated optics," J. Opt. Soc. Am. A **9,** 1289–1300 (1992).

1   Introduction

Telecommunications has continued to push optical fibers towards ever-more demanding applications—such as high bit rates, dense wavelength-division multiplexing (DWDM), and long distances—and in response there has been renewed interest in alternative fiber designs to lift fundamental limitations of silica fibers. A particularly exciting departure from traditional fibers are fibers based on photonic band gaps, forbidden frequency ranges in periodic dielectric structures that can confine light even in low-index or hollow regions [1]. Two main classes of fibers have emerged using photonic band gaps: photonic-crystal "holey" fibers that use a two-dimensional transverse periodicity [2], and Bragg fibers[1] that use a one-dimensional periodicity of concentric rings [3–13]. In this paper, we study the propagation of light in a novel class of Bragg fibers: "OmniGuide" fibers with a hollow core, which use a multilayer cladding that exhibits omnidirectional reflection in the planar limit [7, 10, 14].

In the following sections, we show how OmniGuide fibers bear strong resemblances to the hollow metallic waveguides that are used in the microwave regime, confining a set of guided modes almost entirely within the hollow core with similar field patterns and dispersion characteristics. Because of this strong confinement, we prove that radiation leakage, material absorption, and nonlinearities from the cladding layers can be suppressed by many orders of magnitude. We also study imperfections, such as waveguide bends, acircularity (ellipticity), and surface roughness, and present both general expressions and numerical results for these effects. Moreover, like hollow metallic waveguides, we show that there is substantial loss discrimination between a single lowest-loss mode, TE_{01}, and other guided modes—this produces modal filtering that allows even a highly-multimode OmniGuide fiber to operate in an effectively single-mode fashion. Because this TE_{01} state is cylindrically symmetrical and non-degenerate, it has the additional benefit of immunity to polarization-mode dispersion (PMD) from fiber birefringence. In this way, we demonstrate that OmniGuide fibers have the potential to lift three major physical limitations on silica fibers: losses (currently ~ 0.2 dB/km), nonlinearities, and PMD [15].

One of the hallmarks of photonic crystals is their flexibility, since their optical properties are subject to deliberate structural and materials choices. OmniGuide fibers also embody this freedom, permitting a wide variety of layer-thickness designs to enhance or inhibit specific characteristics (*e.g.* to tailor dispersion parameters), which we do not explore here. Moreover, due to the suppression of cladding properties, a much broader range of materials is available for use than would normally be practical in low-loss optical fibers. In this paper, we describe methods for understanding and designing OmniGuide fiber properties, and especially focus on general scaling laws, phenomena, and design tradeoffs that apply in such systems. For a particular example system, we arbitrarily

---

[1] Bragg fibers should not be confused with fiber Bragg gratings—the former use a lateral index modulation for transverse optical confinement, while the latter use axial modulation for longitudinal confinement and other effects.
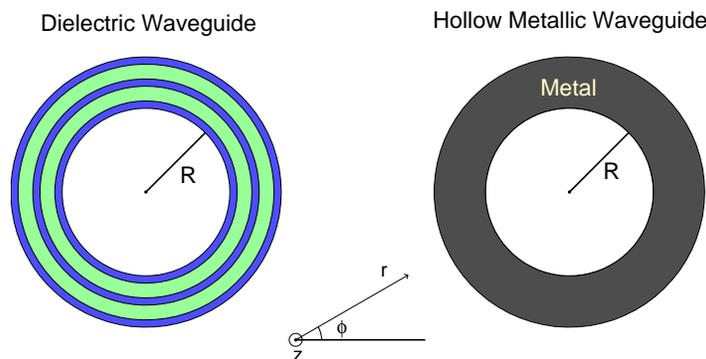
Fig. 1. (a) Hollow dielectric waveguide of radius R. Light is confined in the hollow core by a multilayer dielectric mirror made of alternating layers with high (blue) and low (green) indices of refraction. (b) Hollow metallic waveguide of radius R. Light is confined in the hollow core by a metallic cylinder.

select an index contrast of 4.6 to 1.6 in the cladding, as has been used in several previous publications [7, 10, 11, 13].[2] We explain how the properties scale with the indices in Sec. 10, however, and our scaling laws, analytical techniques, and qualititative results hold true for a wide range of alternative parameters.

2 Hollow Dielectric vs. Metallic Waveguides

In this section, we begin by introducing the basic structure and principles of operation for OmniGuide fibers, and develop an intuition for their behavior by an analogy with hollow metallic waveguides [16,17]. One could also compare with other prior work, including the hybrid system of a metallic waveguide whose inner surface is coated with a multilayer Bragg mirror [18, 19], as well as several other hollow waveguiding systems [20], but the pure metallic guide provides the simplest foundation for understanding. In the left panel of Fig. 1, we depict a schematic of an OmniGuide fiber forming a hollow dielectric waveguide. A hollow core (index of refraction unity) of radius R is surrounded by a multilayer cladding that consists of alternating layers having high and low indices of refraction. The high/low index layers are shown in blue/green. As discussed above, we choose indices of refraction 4.6 and 1.6, with thicknesses here of $0.33a$ and $0.67a$, where a is the thickness of one high/low bilayer (we select different thicknesses in Sec. 2.2). Once a mode frequency ν is computed in units of c/a, the physical value of a is determined via $a = \lambda\nu$ for some desired operational wavelengh λ [1]. The radius R of the waveguide will vary in the differing examples presented in this paper, from a minimum of $2a$ to a maximum of $30a$. In the right panel of Fig. 1, we show a hollow metallic waveguide. The core is the same as that of the hollow dielectric waveguide, but a metal cylinder now replaces the multilayer cladding.

In the metallic case, light is confined in the core by the impenetrability of a near-perfect metal (nonexistent at optical frequencies)—such confined modes for $R = 2a$ are depicted in the right panel of Fig. 2. Dispersions relations like this one depict two conserved quantities: the axial wavenumber β and the frequency ω. In cylindrical waveguides, modes can also be labeled by their "angular momentum" integer m. For waveguides that lie along the z axis, the (z, t, φ) dependence of the modes is then given by: $e^{i(\beta z - \omega t + m\varphi)}$. In a hollow metal tube, the eigenmodes are purely polarized as TM $(H_z = 0)$ or TE $(E_z = 0)$, and the ℓ-th mode of a given m is labeled $\mathrm{T}X_{m\ell}$.

In the dielectric case, light is confined by the one-dimensional photonic band gap of

---

[2]The actual physical indices that we use are currently proprietary.
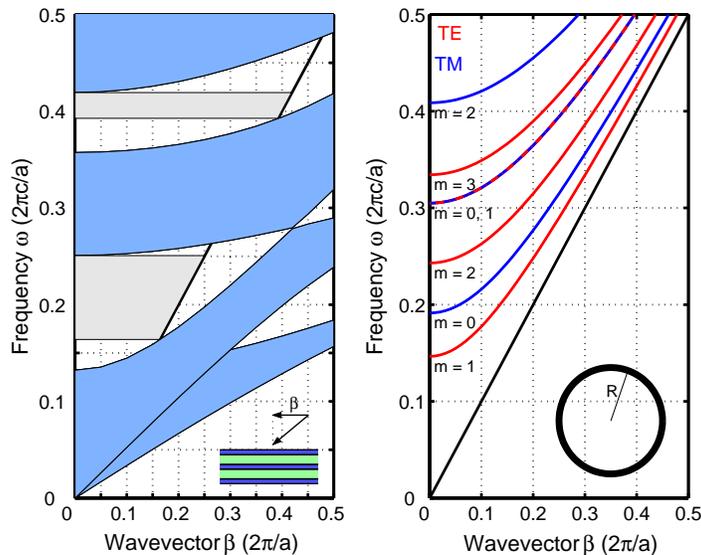
Fig. 2. (Left) Projected band structure associated with the planar dielectric mirror. The blue regions correspond to (β, ω) pairs for which light can propagate within the mirror. White and gray regions correspond to situations where light cannot propagate within the mirror. The thick black line represents the light line ($\omega = c\beta$). Shown in gray are the two omnidirectional frequency ranges of the mirror. (Right) Dispersion relations $\omega(\beta)$ of the lowest 7 modes supported by a hollow metallic waveguide of radius $R = 2a$ are plotted. TE/TM-polarized modes are shown in red/blue, and the modes have angular dependence $e^{im\varphi}$. Note the degeneracy of the TE_{01} and the TM_{11} modes.

the multi-layer cladding, which is easy to analyze in the limit as the cladding becomes planar. The one-dimensional gaps of the planar dielectric mirror structure as a function of β (the surface-parallel wavevector component) are depicted in the left panel of Fig. 2. In these gap regions, we expect the mirrors to behave similarly to a metal, and confine modes strongly analogous to those of the metallic waveguide; this is verified below. Because every eigenmode has a finite, conserved m, the effective wavevector $k_\varphi = m/r$ in the $\hat\varphi$ direction goes to zero for $r \to \infty$. Without this fact, there would be no band gaps in Fig. 2, since nonzero $k_\varphi \perp \beta$ would have to be projected onto the Bragg band diagram. Also shown in this figure, as gray regions, are the ranges of omnidirectional reflection: the frequencies at which *any* incident wave from air will be reflected by the planar mirrors (and vice versa). Omnidirectional reflection *per se* is not strictly necessary for guidance in these fibers, but its presence is strongly correlated with the regimes of large, polarization-independent gaps along the light line that are important for many of the properties studied in this paper.

Bragg mirrors have different band-gaps for "TE" and "TM" polarizations, referring to fields purely parallel to the interface and fields with a normal component, respectively. (Both polarizations are shown in Fig. 2.) This corresponds to the waveguide TE and TM labels only for $m = 0$; all $m \neq 0$ modes have some nonzero E_r component.

2.1 *The modes in an OmniGuide fiber*

The modes supported by any cylindrical waveguide, including metallic waveguides, OmniGuide fibers, and traditional silica fibers, can be computed by the transfer-matrix method of [3]. Here, the longitudinal fields (E_z and H_z) of a given (m, ω, β) in an annular region of index n_j are expanded in Bessel functions $J_m(k_j r)$ and $Y_m(k_j r)$, with
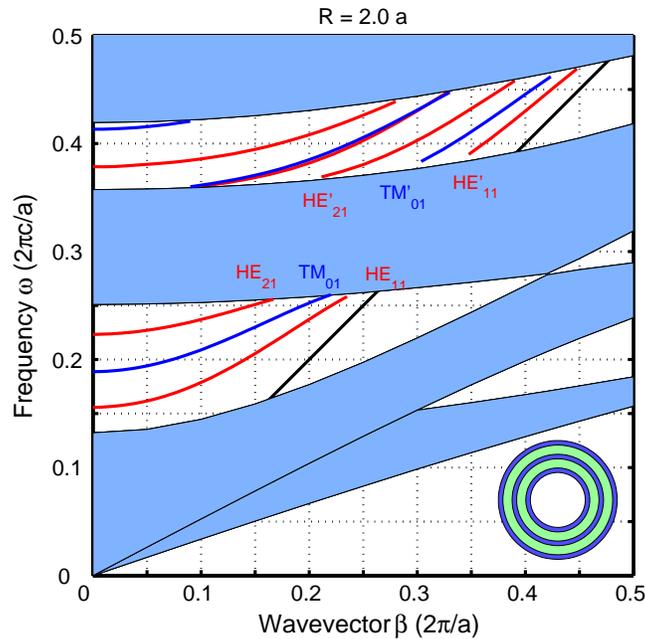
Fig. 3. Guided modes supported by a hollow OmniGuide fiber of radius $R = 2a$: red lines are for TE and HE modes, while blue is for TM and EH modes. In black is the light line ($\omega = c\beta$), and the solid blue regions represent the continuum of modes that propagate within the multilayer cladding. Only the first three modes in each band gap are labeled.

$k_j \equiv \sqrt{n_j^2 \omega^2 / c^2 - \beta^2}$. At each interface, the coefficients are related by a 4×4 transfer matrix that matches boundary conditions.[3] The product of all these transfer matrices yields a single matrix relating the fields in the core to those in the outermost cladding. Then, by application of appropriate boundary conditions, the β_n wavevectors of the various modes can be found; this is discussed in more detail by Sec. 4 below.

Here, we are primarily interested in the modes that lie within the band gap of the one-dimensional Bragg mirrors. Such modes must decay exponentially with r in the cladding, and therefore are truly guided modes in the limit of infinitely many cladding layers (the case of finite layers is considered in Sec. 4). Most of these modes lie above the $\omega = c\beta$ light line, and thus propagate within the hollow core in much the same way as the modes of a metallic waveguide. It is also possible, however, for modes to lie beneath the light line and yet inside the band gap, in which case they are surface states localized around the core/cladding interface—we discuss this possibility further below.

In Fig. 3, we show the computed guided modes of the OmniGuide fiber with core-radius $R = 2a$ and the abovementioned planar-mirror parameters. These modes are at nearly the same frequencies as the metallic waveguide modes of Fig. 2, with the one-dimensional bandgaps simply superimposed. In the dielectric waveguide, the modes are only purely TE and TM for $m = 0$, but for $m \neq 0$ they are strongly TE-like or TM-like, and are called HE and EH, respectively. (When a mode enters the second gap, we add a prime superscript.) Moreover, because these modes are so strongly confined within the core, and have the same orthogonality relationship as in a metal waveguide (see the appendix), the field patterns must also be nearly identical. We consider this analogy in

---

[3]The transfer matrix of Eq. (37) in [3] is erroneous for $m \neq 0$; we hope that this apparent typographical mistake will be corrected by a future erratum.
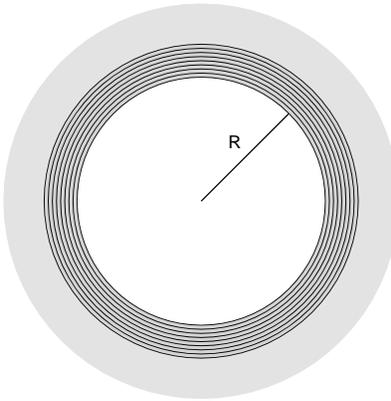
Fig. 4. An OmniGuide fiber with core radius $R = 30a$, the parameters that we employ in the remainder of this paper. The omnidirectional mirror here comprises 17 layers, starting with a high-index layer, with indices 4.6/1.6 and thicknesses $0.22a/0.78a$, respectively. (The omnidirectional mirror is surrounded by some coating for mechanical support; this layer is not shown to scale.) We choose $a = 0.434\mu$m, so that the lowest dissipation losses occur roughly at $\lambda = 1.55\mu$m.

greater detail in a later publication [21], as well as in subsequent sections on losses and bends.

2.2 *A Large-core OmniGuide fiber*

The above calculations yielded the modes of an OmniGuide fiber for a radius $R = 2a$. This small radius has the advantage of supporting only a few modes, which are easy to plot and understand in their entirety, and even has a single-mode frequency range. The analogy with metallic waveguides, however, tells us that this may not be the most desirable regime for fiber operation. In this section, we motivate the use of larger, ostensibly multi-mode cores for OmniGuide fibers, and describe the fiber parameters that we will use for subsequent computations in this paper.

In metallic waveguides, the lowest-loss mode is TE_{01}, and its ohmic losses decrease as $1/R^3$ [16,17]. Moreover, the differential losses between TE_{01} and other modes create a modal-filtering effect that allows these waveguides to operate in an effectively single-mode fashion. On the other hand, for large core radii (high frequencies), losses become dominated by scattering into other closely-spaced modes, especially into the degenerate TM_{11} mode via bends, and it was found that the optimal radius was in the range of $4\lambda - 11\lambda$ [17].

Similar results hold for OmniGuide fibers: the lowest-loss mode is TE_{01}, and many of its losses fall off as $1/R^3$ (for much the same reasons as in metallic waveguides). Like the metallic waveguides, and unlike silica fibers with their small material contrasts, we demonstrate a strong modal-filtering effect based on the degree of confinement in the core. Also as before, inter-modal scattering worsens with increasing R. (We show that bending is less of a problem than in metallic waveguides, however, since the dielectric cladding breaks the TE_{01}/TM_{11} degeneracy.) Thus, for the example OmniGuide fiber that we use in the remainder of this paper, we choose a core radius of $R = 30a$, as depicted in Fig. 4. The point of lowest TE_{01} dissipation losses that we compute in Sec. 6.1 then lies at a frequency of $\omega \cong 0.28 \cdot 2\pi c/a$, so if we make this correspond to the standard $\lambda = 1.55\mu$m of telecommunications, we have $a = 0.434\mu$m. Equivalently, $R = 13.02\mu$m $= 8.4\lambda$, in the favorable range for the metallic-waveguide analogy.[4] Throughout

---

[4]As a positive side-effect, we show that such a core radius brings chromatic dispersion down into a range comparable to that of single-mode silica fibers...although, because of the low nonlinearities, we
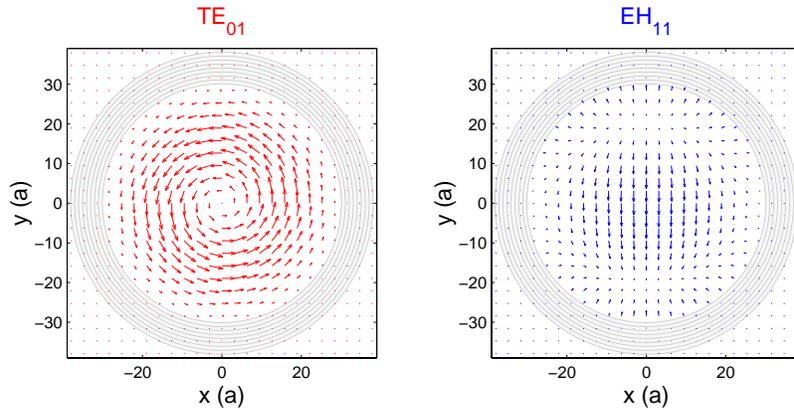
Fig. 5. Transverse electric-field distributions in the OmniGuide fiber of Fig. 4 for the TE_{01} mode (left) and the EH_{11} mode (right), which have $\beta = 0.27926 \cdot 2\pi/a$ and $\beta = 0.27955 \cdot 2\pi/a$, respectively, at $\omega = 0.28 \cdot 2\pi c/a$.

this paper, however, we will emphasize scaling laws with R in order to highlight the effects of differing core sizes.

In order to choose the layer thickness, we employed an approximate quarter-wave condition. It is well-known that, for normal incidence, a maximum band gap is obtained for a "quarter-wave" stack in which each layer has equal optical thickness $\lambda/4$: $d_{\mathrm{hi}}/d_{\mathrm{lo}} = n_{\mathrm{lo}}/n_{\mathrm{hi}}$ [22]. Normal incidence, however, corresponds to $\beta = 0$, whereas the modes of interest in the OmniGuide fiber lie almost on the $\beta = \omega/c$ light line (in the limit of $R \rightarrow \infty$, the lowest-order modes are essentially plane waves propagating along $\hat{z}$). Thus, we employ layer thicknesses determined by the quarter-wave condition along the light line of air (similarly applied in [18]):

$$\frac{d_{\mathrm{hi}}}{d_{\mathrm{lo}}} = \frac{\sqrt{n_{\mathrm{lo}}^2 - 1}}{\sqrt{n_{\mathrm{hi}}^2 - 1}} \tag{1}$$

which yields $d_{\mathrm{hi}} \cong 0.2176a$ and $d_{\mathrm{lo}} \cong 0.7824a$ in this case. (Ref. [3] suggests an alternate method that optimizes the structure for confinement of a given mode, but this yields essentially the same thicknesses as Eq. (1) for large R.)

As in the $R = 2a$ case, the guided-modes of this $R = 30a$ OmniGuide fiber can be labeled by analogy to the modes of an equal-radius metallic waveguide. Two such modes in the OmniGuide fiber, the lowest-loss TE_{01} and the linearly-polarized[5] EH_{11} (analogous to the TM_{11} mode in a metallic guide) are depicted in Fig. 5. The TE_{01} mode is circularly symmetric and "azimuthally" polarized ($\vec{E} \| \hat{\varphi}$)—thus, unlike the doubly-degenerate EH_{11} mode (two orthogonal polarizations), TE_{01} cannot be split into two modes of differing velocities by fiber imperfections, and is therefore immune to polarization-mode dispersion (PMD). (See also Sec. 8.) Actually, the mode labeling in an OmniGuide fiber is more complex than in a metallic waveguide, because sometimes a mode will cross the light line and become a surface state localized around the core/cladding interface. When that happens, another mode moves "up" and takes its place; for example, the TM_{01} mode crosses the light line at $\omega \cong 0.27 \cdot 2\pi c/a$, while the TM_{02} mode continuously takes on the core field pattern of TM_{01}. When in doubt, we label a mode as HE or EH

shall argue that such a correspondence is not strictly necessary.

[5]With our choice of $e^{im\varphi}$ φ-dependence, the EH_{11} mode is actually circularly polarized; combined with its degenerate $m = -1$ mode, however, one can instead express it as linearly polarized.
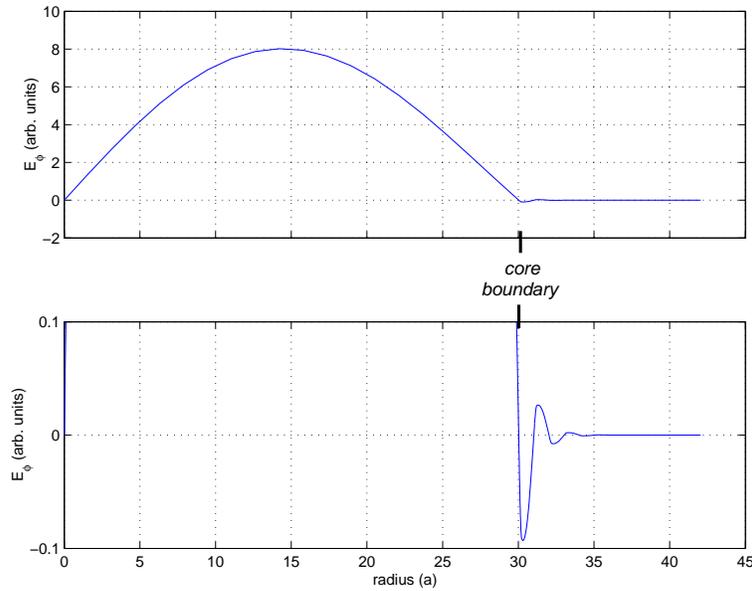
Fig. 6. The (unnormalized) electric field E_φ for the TE_{01} mode in the OmniGuide fiber of Fig. 4. The lower plot displays the same field, but with the vertical scale exaggerated in order to show the field amplitude in the cladding. The field has a node near the core interface at R, and so the field amplitude in the cladding is determined by the slope at that point.

depending upon whether it is dominated by H_z or E_z at $r = 0$, respectively, and number the core modes according to their ordering above the light line.

3   Scaling Laws with Core Size

Because of the strong reflectivity of the dielectric mirrors, many of the mode properties are determined largely by the geometric size R of the core, within which the modes are confined. Throughout this paper, we thereby derive scaling relations for the different quantities computed, and in this section we lay the groundwork for those derivations by presenting basic scalings of the fields and modes. These scaling relations are largely independent of details such as the precise index contrast that is used, so long as it is sufficiently large for the metallic analogy to hold, and will provide a broad understanding of the advantages and tradeoffs of OmniGuide fiber structures. Later in the paper, we exhibit data to explicitly verify scaling relations derived from those in this section.

In particular, we will focus on the suppression of cladding phenomena for the $TE_{0\ell}$ (especially TE_{01}) modes of the fiber. The critical property of $TE_{0\ell}$ modes is that, by analogy with a hollow metallic waveguide, they have a node in their electric field (E_φ) near $r = R$ [16, 17] as depicted in Fig. 6. It then follows that the amplitude of the electric field in the cladding is proportional to the *slope* of E_φ at R. The form of E_φ in the core, however, is simply the Bessel function $J_1(\xi r/R)$, where $\xi(\omega)$ is roughly the ℓ-th zero of J_1. The slope at R is then $(J_0(\xi) - J_2(\xi)) \cdot \xi/2R$. Moreover, for our quarter-wave stack, E_φ peaks near each of the $n_{hi} \to n_{lo}$ interfaces [3]. Thus, not including any normalization of the J_1 amplitude (*i.e.* $E_\varphi \sim 1$), we find that the *unnormalized* E_φ in the cladding scales as d_{hi}/R. In addition, for most computations (such as the perturbation theory described in the appendix), one must normalize the power of the field: this means dividing $\vec{E}$ by an additional factor proportional to $\sqrt{\text{mode area}} \sim R$,

and so:

$$\text{normalized } \text{TE}_{0\ell} \text{ cladding } \vec{E} \sim \frac{1}{R^2}. \tag{2}$$

Moreover, the area of the field in the cladding is the perimeter $\sim R$ times some constant (penetration depth) that depends on the size of the band gap; combined with Eq. (2), we therefore find:

$$\text{fraction of } \int |\vec{E}|^2 \text{ in cladding for } \text{TE}_{0\ell} \sim \frac{1}{R^3}, \tag{3}$$

and from this we derive many other scaling relations. In contrast, for TM or mixed-polarization modes with an E_r component, the unnormalized field amplitude in the cladding remains roughly constant with changing R—their fractional $|\vec{E}|^2$ in the cladding then scales as only $1/R$, so the cladding has a much greater effect on them.

By general phase-space arguments, the total number of modes in the core must scale as the area R^2. Moreover, in a metal waveguide, the dispersion relations look like $\beta_n = \sqrt{\omega^2/c^2 - \xi_n^2/R^2}$, where ξ_n are roots or extrema of Bessel functions. Therefore, far from cutoff ($R \gg \xi_n c/\omega$),

$$\text{mode separation } \Delta\beta \sim \frac{1}{R^2}; \tag{4}$$

this has important implications for many of the mode-coupling phenomena discussed later. Unfortunately, $\Delta\beta$ can be somewhat more complicated in an OmniGuide fiber, due to the finite field penetration into the cladding and due to the transitions into surface states and subsequent mode relabelings discussed in the previous section. For example, consider the case of the EH_{11} mode, which is degenerate with TE_{01} in the metallic limit [16, 17]. The degeneracy is broken by the penetration of the fields into the cladding,[6] inducing a small shift $\Delta\beta$: by perturbation theory, $\Delta\beta$ is proportional to the amount of EH_{11} energy in the cladding, $\sim 1/R$:

$$\text{TE}_{01} \text{ and } \text{EH}_{11} \text{ mode separation } \Delta\beta \sim \frac{1}{R}. \tag{5}$$

Testing this scaling relation numerically for $\lambda = 1.55\mu\text{m}$, however, we find that this separation eventually scales as $1/R^2$ for $R \gtrsim 40a$. It turns out that the "fundamental" HE_{11} mode has crossed the light line to become a surface state, and EH_{11} continuously transitions to being more HE_{11}-like, thus scaling eventually as Eq. (4).

4 Leaky Modes and Radiation Loss

In the preceding discussion, we have neglected a point that may seem important: in reality, there will be only a finite number of cladding layers in the omnidirectional mirror. Because of this, and the fact that the modes of interest lie above the light line of the outermost region, the field power will slowly leak out in a process akin to quantum-mechanical "tunneling." This radiation loss, however, decreases exponentially with the number of cladding layers, and we quantify its smallness explicitly below. As has been observed elsewhere [11, 13], we show that only a small number of layers is required to achieve leakage rates well below 0.1 dB/km. Moreover, the radiation leakage strongly differs between modes, inducing a modal-filtering effect [3, 6] that allows a large-core OmniGuide fiber to operate in an effectively single-mode fashion.

In the limit of infinitely many cladding layers, the modes in the OmniGuide core are true confined modes, thanks to the band gap, with discrete real eigenvalues β_n

---

[6]Such degeneracy breaking can also be understood in terms of the phase shift of a TE/TM polarized wave upon reflection from the omnidirectional mirror [21].

(*c.f.* the appendix). For finitely many layers, modes are no longer truly confined (above the outermost light line), leading to a continuum of β values with infinitely-extended eigenstates [3]. The former confined modes become leaky *resonances*: superpositions of real-β eigenmodes centered on β_n with a width $\Delta\beta$ proportional to the radiative decay rate α_n. Such resonances can be studied directly via the physical real-β continuum, but a powerful alternative method is the leaky-mode technique, which employs a conceptual analytic continuation from β to $\widetilde{\beta}$ in the complex plane to satisfy a boundary condition of zero incoming flux [23]. The power decay rate α_n is then given by $2\Im[\widetilde{\beta}_n]$, where $\Im$ denotes the imaginary part; we have also verified the correctness of this decay rate against explicit real-β superpositions as well as by beam-propagation methods (BPM) [24].

For an OmniGuide fiber, the leaky-mode method is as follows. The transfer-matrix formulation allows one to compute 2×2 matrices $M_m^{\pm}(\omega, \beta)$ that connect the TE and TM amplitudes at the origin to the amplitudes of the outgoing $(+)$ or incoming $(-)$ TE and TM cylindrical waves (Hankel functions) in the outermost region, as a function of ω and β for a given angular-momentum index m. (For $m = 0$, the two polarizations decouple [3].) For a leaky mode, we wish to impose the boundary condition of zero incoming waves, so that there are no sources at ∞; such a solution exists whenever there is a zero eigenvalue of M_m^-. Therefore, we use the determinant:

$$f_m(\omega, \widetilde{\beta}) \equiv \det\left[\mathrm{M}_m^-(\omega, \widetilde{\beta})\right],\qquad(6)$$

so that the leaky mode is defined by $f_m(\omega, \widetilde{\beta}_n) = 0$. Once such a $\widetilde{\beta}_n$ is found for a given ω, the corresponding eigenvector of $M_m^-(\omega, \widetilde{\beta}_n)$ yields the required mixed-polarization amplitudes. With finitely many layers, the only real roots of f_m lie below the light line of the outermost region;[7] above this light line, the incoming and outgoing flux are equal for real β [3], corresponding to steady-state standing-wave patterns. The small imaginary part of $\widetilde{\beta}_n$ above the light line yields the power decay rate $\alpha_n = 2\Im[\widetilde{\beta}_n]$. A similar leaky-mode method was previously used for Bragg fibers, albeit with only a first-order Taylor-expansion approximation for $\Im[\widetilde{\beta}_n]$ [5].

For all modes, the radiative decay α decreases exponentially with increasing numbers of cladding layers, thanks to the exponential decay of fields in the Bragg band gap, eventually to the point where other losses (*e.g.* absorption) dominate. At $\lambda = 1.55\mu$m for this structure, the TE/TM losses decrease by a factor of $\sim 10/5$ per cladding bilayer, respectively. Because of the smaller TM band gap, the losses of mixed-polarization $(m \neq 0)$ modes are eventually dominated by their less-confined TM components. In Fig. 7, we display the computed radiation leakage rates α for the lowest-loss TE_{01} mode, the next-lowest loss TE_{02} mode, and the linearly-polarized EH_{11} mode to typify mixed-polarization modes. Like the absorption discussed later, these differential losses create a mode-filtering effect that allows the TE_{01} mode to operate as effectively single-mode, even for large-core OmniGuide fibers, a fact that was also noted in [3,6]. A similar principle was employed in hollow metallic waveguides [16,17] to select the TE_{01} mode. Note that, as in metallic waveguides, TE_{02} is not necessarily the mode of greatest concern—it is more important to consider modes that couple strongly to TE_{01} via perturbations, such as those discussed in later sections. From Fig. 7, it is seen that with only 17 cladding layers the TE_{01} mode has leakage rates well under 0.01 dB/km, and even EH_{11} has decay lengths of meters, corresponding to $\Im[\widetilde{\beta}_n]/\Re[\widetilde{\beta}_n]$ of $\sim 10^{-13}$ and $\sim 10^{-9}$, respectively. Thanks to these low losses, the modes can be treated as truly

---

[7]Below the light line of the outermost region, the incoming-wave Hankel function instead becomes an exponentially-growing function, but its coefficient must be zero all the same.
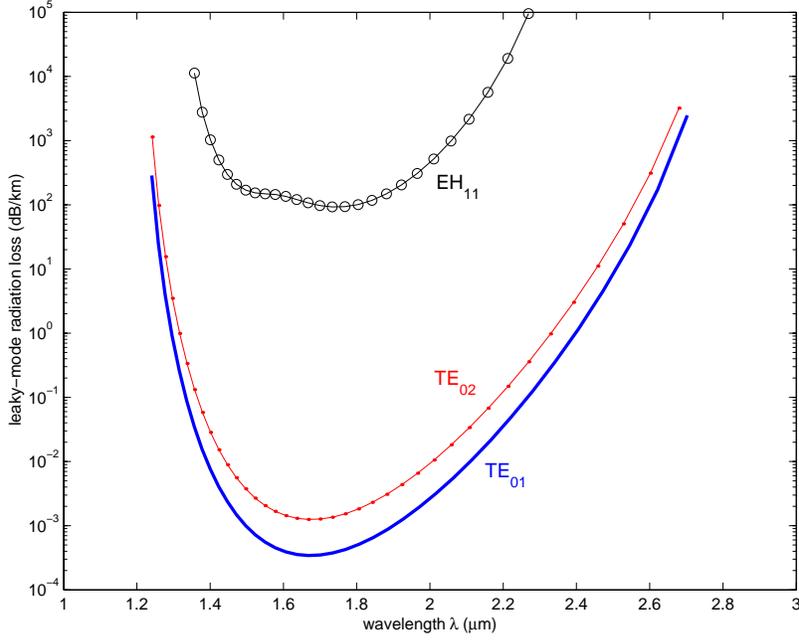
Fig. 7. Radiation leakage through a finite number (17) of cladding layers in the OmniGuide fiber of Fig. 4. The lowest-loss mode is TE_{01} (solid blue) and the next-lowest is TE_{02} (red dots), while the linearly-polarized EH_{11} mode (black circles) typifies the higher losses for mixed-polarization modes due to the smaller TM band gap.

bound for most analyses (*e.g.* dispersion relations and perturbation theory), with the leakage rates at most included as an independent loss term.

The radiation losses are proportional to the field amplitude $|\vec{E}|^2$ in the cladding, which goes like $1/R^4$ for $TE_{0\ell}$ from Eq. (2), multiplied by the surface area (which scales as R). Thus,

$$TE_{0\ell} \text{ radiation leakage } \alpha \sim 1/R^3, \tag{7}$$

the same as the scaling of $TE_{0\ell}$ ohmic losses in a hollow metallic waveguide [16, 17]. In contrast, because of their lack of a node near the boundary, TM and mixed-polarization radiation losses scale only as $1/R$.

By conservation of energy, one can also express this α_n as $\widetilde{P}_n^+/\widetilde{P}_n$, where $\widetilde{P}_n^+$ is the radially-outgoing power of the leaky mode per unit length and $\widetilde{P}_n$ is its forward-propagating power in the core. It has been suggested [13] that one instead use $\alpha_n' \equiv P_n^+/P_n$ based on the powers at the real-β_n resonance peak, but one can show that this formulation is too small by a factor of 4. In particular, denote the outgoing/incoming wave amplitudes at ω by $S^\pm(\beta)$. From above, S^- has a root at $\widetilde{\beta}_n \cong \beta_n + i\alpha/2$, so S^- can be Taylor-expanded: $S^-(\beta) \cong s \cdot (\beta - \beta_n - i\alpha/2)$ for some s. The outgoing amplitude S^+ can then be inferred by time-reversal symmetry, $S^+(\beta) \cong s^* \cdot (\beta - \beta_n + i\alpha/2)$, and so we see immediately that $\widetilde{P}_n^+ \sim |S^+(\beta_n + i\alpha/2)|^2 \cong 4|S^+(\beta_n)|^2 \sim 4P_n^+$, and thus $\alpha \cong 4\alpha'$. (We have also verified this factor of 4 by explicit computation of fluxes.)
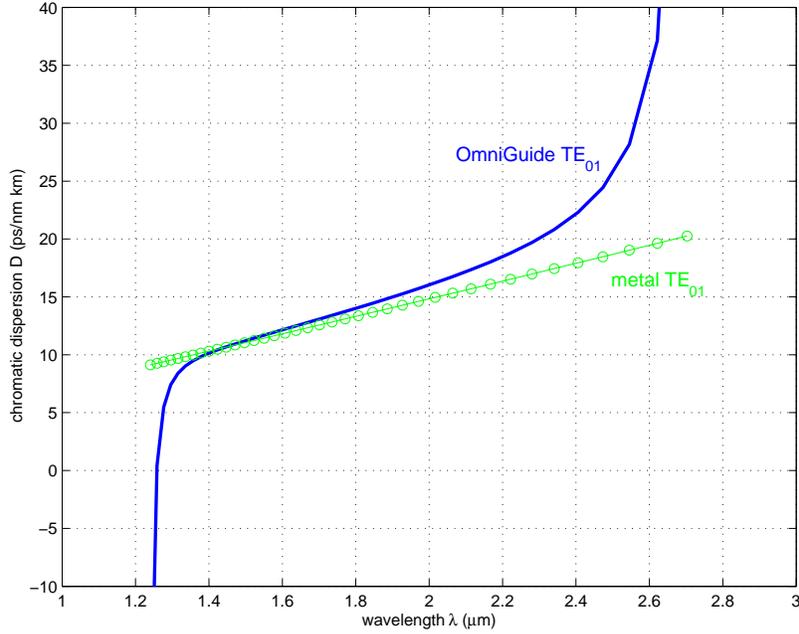
Fig. 8. Group-velocity (chromatic) dispersion of the TE_{01} mode in both the OmniGuide fiber of Fig. 4 (solid blue) and a hollow metallic waveguide with the same core radius (green circles).

5 Group-velocity Dispersion

Given a dispersion relation $\beta(\omega)$, one important quantity is the group-velocity dispersion D (the rate at which pulses spread), canonically defined as [15]:

$$D \equiv -\frac{\omega^2}{2\pi c}\frac{d^2\beta}{d\omega^2}, \tag{8}$$

in units of ps/(nm · km): the pulse-spreading (ps) per km of propagation per nm of $\Delta\lambda$. This can be computed exactly from the function f of Eq. (6), which defines the dispersion relation implicitly by $f(\omega, \beta) = 0$. The group velocity is thus given by $v \equiv d\omega/d\beta = -f_\beta/f_\omega$, where the subscripts denote partial differentiation, and one thereby finds that $d^2\beta/d\omega^2 = d(1/v)/d\omega = 2f_\omega f_{\omega\beta}/f_\beta^2 - f_{\omega\omega}/f_\beta - f_\omega^2 f_{\beta\beta}/f_\beta^3$. We evaluate all of these derivatives analytically by differentiating the transfer matrices. We also considered material dispersion (n varying with ω) by the same methods, but we found that this has a negligible effect (due to the small field penetration into the cladding). For example, assuming that the cladding has the same $dn/d\omega$ and $d^2n/d\omega^2$ as silica at $1.55\mu m$, the contribution of material dispersion is less than 0.1 ps/(nm · km) over most of the bandwidth. What remains is the waveguide dispersion, which stems from the geometry of the core as well as the variable penetrability of the cladding, Goos-Hänchen shifts [22], *etc.*, all of which are taken into account by differentiating f. The resulting dispersion as a function of wavelength is plotted in Fig. 8 for the TE_{01} mode of the $R = 30a$ OmniGuide fiber.

For comparison, we also plot the dispersion of the TE_{01} mode in an equal-radius hollow metallic waveguide, given by: $D_{\mathrm{metal}} = -\omega^2\xi^2/(2\pi c^3\beta^3 R^2)$, where $\beta = \sqrt{\omega^2/c^2 + \xi^2/R^2}$ and $\xi = 3.8317\cdots$ is the first non-zero root of the J_1 Bessel function. Except near the edges of the band gap, the dispersion is very similar to that of the metallic waveguide— that is, D is dominated simply by the core shape—and $D \cong 12$ ps/nm · km at $\lambda = 1.55\mu m$. From the metallic dispersion relation, we can also conclude that $D \sim 1/R^2$.

As we discuss in the next section, the practical implications of dispersion in an OmniGuide fiber are quite different than in ordinary fibers, due to the absence of nonlinear effects. Because dispersion no longer interacts with nonlinearities, it can in principle be completely compensated after any distance of propagation, allowing one to put all dispersion compensation at the end of a fiber link, as well as to tolerate higher dispersions. Conversely, operating at or near a point of zero dispersion will no longer exacerbate four-wave mixing noise.

Another important consideration is the relative dispersion slope (RDS), as measured by $(dD/d\lambda)/D$; this quantity must ideally be matched in any dispersion-compensation system. For the OmniGuide fiber above, the RDS is around 0.0007nm^{-1}. This is 15–30 times smaller than the RDS of contemporary TrueWave-RS (0.010nm^{-1}) and LEAF (0.021nm^{-1}) fibers, and smaller slopes are typically easier to achieve in dispersion-compensating fibers [25].

6 Suppression of Absorption and Nonlinearities

In this section, we compute the effect of absorption losses and nonlinearities in the cladding materials of an OmniGuide fiber. We show that these effects are strongly suppressed for the TE_{01} mode, allowing highly lossy and nonlinear materials to be employed—greatly broadening one's choices for high-index materials. Moreover, we will see that there is the potential of greatly surpassing even the properties of silica fibers.

Absorption and nonlinearites correspond to tiny shifts $\Delta\varepsilon$ in the dielectric constant of the materials, and can therefore be treated by perturbation theory, as described in detail by the appendix. This common technique allows one to compute the shift $\Delta\beta$ due to a small perturbation, using only the unperturbed modes (computed earlier via transfer matrices). We have developed a new formulation of perturbation theory for use in this and subsequent sections, in explicit analogy with quantum mechanics, and use the Dirac notation $\hat{A}\,|n\rangle = \beta_n \hat{B}\,|n\rangle$ for the vectorial Maxwell eigenproblem in the modes $|n\rangle$. A perturbation is expressed as a shift $\Delta\hat{A}$ in the eigen-operator, and the first-order shift in β is then $\Delta\beta_n^{(1)} = \langle n|\Delta\hat{A}|n\rangle$ from Eq. (43). The $\Delta\hat{A}$ for a small $\Delta\varepsilon$ is given by Eq. (48) in the appendix.

6.1 *Absorption Loss*

For absorption losses (also possibly including Rayleigh scattering), $\Delta\varepsilon$ is a small imaginary part added to ε, representing the (material-dependent) dissipation rate. Substituting Eq. (48) into Eq. (43), the resulting (purely imaginary) $\Delta\beta$ indicates the decay rate of the mode. Such a first-order perturbation method for dissipation losses, derived by various means, has often appeared in previous works [26–31]. The losses of a material are usually specified as a power dissipation rate α_0 in units of *e.g.* dB/m; after some algebra, one finds that using $\Delta\varepsilon = i\alpha_0 \cdot 2c\sqrt{\varepsilon}/\omega$ produces an $\Im[\Delta\beta^{(1)}]$ in Eq. (43) that is exactly the power dissipation rate α in the same units as α_0.

Here, we calculate the losses of the TE_{01} mode in our example OmniGuide fiber by assuming that the core is lossless, and that both the high and low-index cladding materials have the same dissipation rate α_0. Furthermore, we divide the computed dissipation rate α by α_0, yielding the dimensionless, material-loss independent *absorption suppression* coefficient of the mode. This is done for each frequency ω across the band gap, yielding the plot in Fig. 9. Thus, the cladding losses are suppressed by more than four orders of magnitude over most of the bandwidth, a result that will be better understood from the scaling-law arguments in Sec. 6.3. For comparison, we also show the next-lowest loss TE_{02} mode, as well as the linearly-polarized EH_{11} (exemplifying the larger cladding
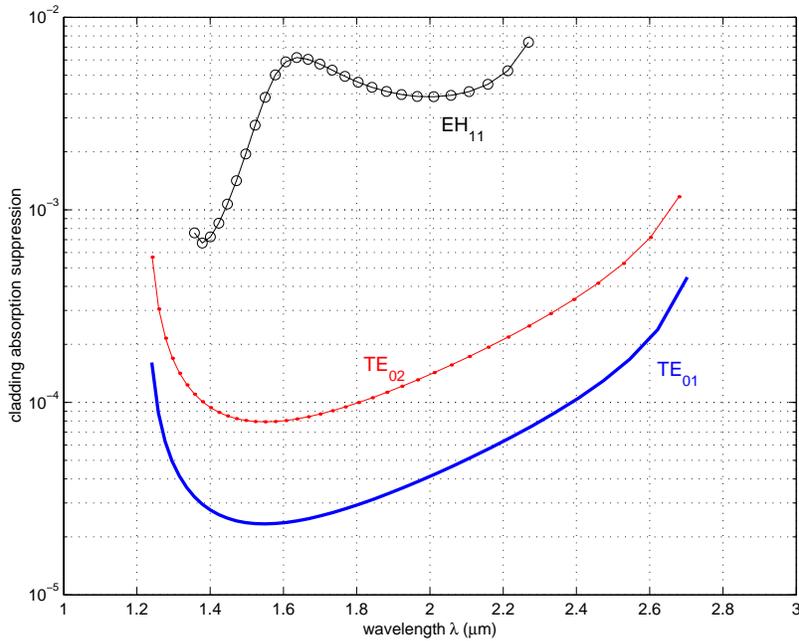
Fig. 9. Absorption losses due to the cladding materials the OmniGuide fiber (with core radius $30a$), as a fraction of the bulk cladding losses. The lowest-loss mode is TE_{01} (solid blue) and the next-lowest is TE_{02} (red dots), while the linearly-polarized EH_{11} mode (black circles) typifies the higher losses for mixed-polarization modes due to the smaller TM band gap.

penetration for modes with TM components).[8] As was mentioned earlier, such a loss differential creates a mode-filtering effect that should allow single-mode-like operation.[9] (Surface states and guided modes outside the band gap, *i.e.* propagating within the cladding region, will experience essentially the attenuation of the bulk cladding materials and will be even more strongly filtered out.) Moreover, even if the cladding has losses a thousand times greater than silica's ~ 0.2 dB/km, the TE_{01} losses can be lower than the losses of silica fibers.

6.2 *Nonlinearities*

Another important problem in optical fibers is that of Kerr nonlinearities. Here, the index n of the material varies as a function of electric-field strength: $n' \equiv n + n_2|\vec{E}|^2$, where $n_2 = \frac{3}{8n}\chi^{(3)}$ is the (small) "nonlinear index coefficient" of the material(s).[10] Thus, to first order in n_2, one has:

$$\Delta\varepsilon = 2nn_2\left|\vec{E}\right|^2. \tag{9}$$

Kerr nonlinearities cause several problems in fiber systems: self/cross-phase modulation (SPM/XPM), where the energy at one frequency shifts the β at the same/another frequency; and also four-wave mixing (FWM), in which energy at one frequency leaks

---

[8]The strange shape of the EH_{11} curve in the plot is related to the fact that this mode labeling is not exact for OmniGuide fibers; in fact, "EH_{11}" begins to make a transition to HE_{11}-like behavior in the middle of the band.

[9]Bessel-function afficionados can also show that the ratio of $TE_{0\ell}$ to $TE_{0\ell'}$ losses is nearly $(\xi_\ell/\xi_{\ell'})^2$, where ξ_ℓ and $\xi_{\ell'}$ are the corresponding roots of J_1. This ratio is ~ 3.35 for TE_{02} to TE_{01}.

[10]Often, one instead uses $n' = n + n_2I$, where $I \sim n|\vec{E}|^2$ is the intensity of light; our analysis remains the same except for the extra factor of n.
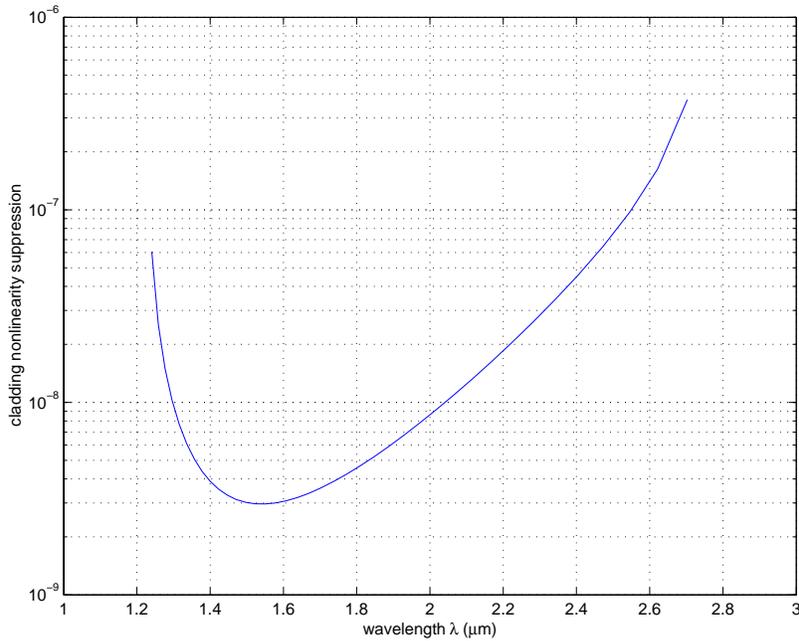
Fig. 10. The TE$_{01}$ mode's suppression factor for cladding nonlinearities in the Om-
niGuide fiber of Fig. 4, relative to nonlinearities that include the core.

into another frequency [15]. SPM and XPM interact with dispersion to limit dispersion-
compensation schemes, and FWM causes noise/crosstalk between channels. Our concern
here is not to compute these effects *per se*, but rather to define the limits in which they
may be neglected.

The strength of nonlinearities in a fiber is given by a nonlinear lengthscale L_{NL},
defined as the inverse of the SPM phase shift $\Delta\beta$; this is the lengthscale at which SPM
and XPM become significant, and also appears as a scaling coefficient in the FWM noise
[15]. As is seen below, L_{NL} is inversely proportional to the mode power P (to first order),
so it is conventional to instead define the nonlinear strength $\gamma \equiv 1/(PL_{NL}) = \Delta\beta/P$,
which is a power-independent quantity proportional to the strength of nonlinear effects
in the fiber.

In order to compute γ, we substitute Eq. (9) into Eqs. (48,43), solving for the first-
order shift $\Delta\beta^{(1)}$. This $\Delta\beta^{(1)}$ is proportional to P through the field strength $|\vec{E}|^2$ in
Eq. (9). (An equivalent expression was derived by other means, for both the scalar and
vectorial cases, in previous works [32–34].)

We now apply the above methods to compute the nonlinear strength γ of the TE$_{01}$
mode in our OmniGuide fiber, assuming that the cladding materials all have some
fixed n_2. Instead of choosing a particular material n_2, we instead calculate a cladding
nonlinearity suppression factor—we divide γ by a γ_0, with the latter computed by
supposing that both the cladding *and* the core have the n_2 nonlinearity. The results,
plotted in Fig. 10, show that the cladding nonlinearities are suppressed by more than
eight orders of magnitude over much of the bandwidth. Thus, the nonlinearities of this
OmniGuide fiber will be dominated by the nonlinearities of *air* rather than those of
the cladding, even for materials thousands of times more nonlinear than silica. Gases
have Kerr constants almost 1000 times weaker than that of silica—combined with the
fact that the core area here is almost 10 times larger than the effective area of a typical
silica fiber, this implies nonlinearities in the OmniGuide fiber that are almost 10,000

times weaker than those of silica fibers. Such low nonlinearities would open dramatically new areas for fiber operation: for example, high powers, closely-spaced channels and/or low/zero dispersion without regard for FWM,[11] use of non return-to-zero (NRZ) formats at high bit rates, and dispersion compensation at larger intervals without regard for SPM. A better understanding of this nonlinearity suppression can be found in the scaling laws derived in the following section.

6.3 *Scaling Laws*

The scaling laws for absorption loss and nonlinearities, as a function of core radius R, can be derived straightforwardly from the results in Sec. 3. In particular, the $\langle n|\Delta\hat{A}|n\rangle$ integral that determines the absorption loss has an integrand proportional to the fraction of $|\vec{E}|^2$ in the cladding, which scales as $1/R^3$ from Eq. (3), so:

$$\text{TE}_{0\ell} \text{ cladding absorption} \sim \frac{1}{R^3}. \tag{10}$$

This is a familiar result, since it is the same as the scaling of the TE_{01} ohmic dissipation losses in a hollow metallic waveguide. The scaling for the nonlinear strength γ is found by similar arguments. Here, however, there is an additional factor of $|\vec{E}|^2$ from Eq. (9), and thus $1/R^4$ from Eq. (2). The nonlinear strength γ of the cladding therefore scales like $1/R^7$! The nonlinear strength γ_0, when one adds nonlinearities to the core, scales inversely with the area R^2 as in an ordinary fiber, so:

$$\text{TE}_{0\ell} \text{ cladding nonlinearity } \frac{\gamma}{\gamma_0} \sim \frac{1}{R^5}. \tag{11}$$

It is because of these rapid $1/R^3$ and $1/R^5$ scalings that the cladding absorption and nonlinearities can be suppressed so strongly for TE_{01} in a large-core OmniGuide fiber. To demonstrate these scaling laws explicitly, we plot the absorption and nonlinear suppression coefficients as a function of R in Fig. 11, superimposing the predicted scaling laws.

7 Waveguide Bends

A shallow bend in the waveguide axis, with unchanged waveguide cross-section[12] and an instantaneous radius of curvature $R_b \gg R$, can be thought of as a small perturbation to the straight waveguide. The modes of the straight waveguide propagate almost unchanged around the bend, with a slight coupling between them due to the bending—such coupling, or scattering, is described via the z-dependent perturbation theory of the appendix. After computing the strength of such coupling terms, we first consider mode conversion due to coupling of guided modes for short bends in which they are effectively lossless. Then, in Sec. 7.3, we consider the effect of coupling to lossy modes over longer distances, which causes an effectively increased loss rate for TE_{01}.

7.1 *The Bend Perturbation Operator*

The unperturbed eigenmodes are coupled in a bend by the change $\Delta\hat{A}$ in the eigen-operator, produced by transforming the field-propagation equations into the curvilinear coordinates of the bend. In order to find the propagation equations for the field on the

---

[11]FWM noise is proportional to $\gamma^2/(\Delta\beta^2 + \alpha^2)$, where the α^2 term is usually negligible [15]. However, with nonlinearities 10,000 times weaker than in silica, $\alpha = 0.01$ dB/km is sufficient to suppress FWM even in the limit of $\Delta\beta = 0$ (zero dispersion and/or channel spacing).

[12]Bending can also create a stress-induced $\Delta\varepsilon$ in the cladding material, which we do not consider here since so little of our field penetrates into the cladding.
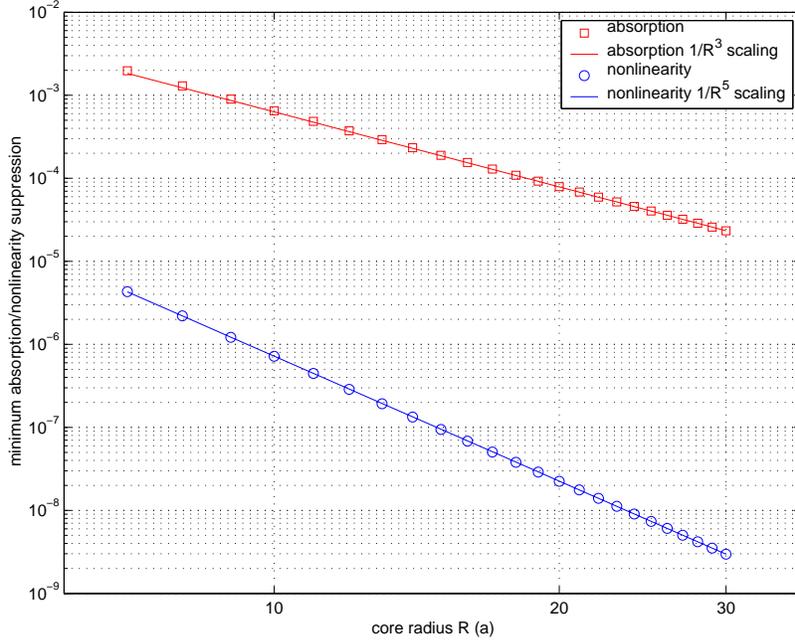
Fig. 11. Scaling of the cladding absorption and nonlinearity suppression factors for a core radius R varying from $7a$ to $30a$ (taking the minimum over the TE_{01} band at each radius). Hollow squares/circles show the computed values, and the solid lines display the values predicted by starting from the $30a$ value and applying the scaling laws.

cross-section of a curved waveguide, we write Maxwell's equations in cylindrical coordinates (ρ, θ, ζ), make the correspondence $(x, y, z) \rightarrow (R_b - \rho, \zeta, R\theta)$ where $-\hat{x}$ points to the center of curvature and $x = 0$ bisects the waveguide, and recompute Eq. (38) of the appendix. Then, after some algebra, we find the mode-coupling coefficient:

$$
\left\langle n' \left| \Delta \hat{A} \right| n \right\rangle = - \left\langle
\begin{array}{c}
E'_x \\
E'_y \\
E'_z \\
H'_z \\
H'_y \\
H'_z
\end{array}
\left|
\frac{\omega x}{c R_b}
\begin{pmatrix}
\varepsilon & & & & & \\
& \varepsilon & & & & \\
& & -\varepsilon & & & \\
& & & \mu & & \\
& & & & \mu & \\
& & & & & -\mu
\end{pmatrix}
\right|
\begin{array}{c}
E_x \\
E_y \\
E_z \\
H_z \\
H_y \\
H_z
\end{array}
\right\rangle
\tag{12}
$$

As far as we can determine, this diagonal form for the bend-coupling operator was not previously known—although with some effort it can be shown to be equivalent to expressions derived by other means in earlier works, for example [35]:

$$
\begin{aligned}
\left\langle n \left| \Delta \hat{A} \right| n' \right\rangle &= -\beta_{n'} \int \frac{x}{R_b} \left(\vec{E}_t^* \times \vec{H}_t' + \vec{E}_t' \times \vec{H}_t^* \right) \\
&\quad - \frac{i}{R_b} \int \left(E_y^* H_z' - H_y^* E_z' \right).
\end{aligned}
\tag{13}
$$

The simple form of Eq. (12), cast into cylindrical coordinates $x = r \cos \varphi$, immediately yields a well-known result when the waveguide has cylindrical symmetry. Here, the modes can be chosen with a φ dependence of the form $e^{im\varphi}$, so:

$$
\begin{aligned}
\left\langle n'; m' \left| \Delta \hat{A} \right| n; m \right\rangle &= (r \text{ integral}) \cdot \int_0^{2\pi} e^{i\Delta m \varphi} \left(e^{i\varphi} + e^{-i\varphi} \right) d\varphi / 4\pi \\
&= (r \text{ integral}) \cdot \delta_{\Delta m, \pm 1} / 2,
\end{aligned}
\tag{14}
$$

where $\Delta m = m - m'$. In other words, for a waveguide with a cylindrical symmetry, there is a *selection rule*: a bend can only *directly* couple modes with $|\Delta m| = 1$ [35]. From this selection rule, it follows that a mode cannot couple with itself, and the lowest-order correction to β is therefore of order $1/R_b^2$, from Eq. (44) [36].

7.2   *Bends in an OmniGuide Fiber*

In a conventional optical fiber, there is only a single guided mode, so all of the coupling in a bend is to the radiation continuum, which lies at a nearby β since the index-contrast is small. In contrast, the OmniGuide fiber here is highly multi-mode, with many other guided modes at β values nearby to TE_{01} (within $\Delta\beta = 10^{-3} \cdot 2\pi/a$); at the same time, the cladding modes (analogous to the radiation continuum) lie at distant β ($\Delta\beta \gtrsim 0.1 \cdot 2\pi/a$) thanks to the large gap. Thus, since mode coupling varies inversely with $\Delta\beta$, OmniGuide-fiber bend effects will be dominated by coupling/scattering into other guided modes in the core. In this case, we can employ Eq. (46) to compute the scattered power, which is therefore proportional to $(R_b\Delta\beta)^{-2}$. This scattered power will be dominated by the closest $m = 1$ mode, and is significant when R_b approaches $1/\Delta\beta$.

Moreover, we can be guided once again by the analogy with hollow metallic waveguides. There, as was discussed in Sec. 3, the TE_{01} mode is actually *degenerate* ($\Delta\beta = 0$) with another mode, TM_{11}. The selection rule allows these two modes to couple, and therefore can produce significant scattering for *any* bend radius. Fortunately, the OmniGuide cladding breaks this degeneracy, but the strongest scattering is still commonly due to the EH_{11} mode (the analogue of TM_{11}), which has a $\Delta\beta \sim 10^{-4} \cdot 2\pi/a \sim 10 \text{cm}^{-1}$ for $R = 30a$. Actually, even in the OmniGuide fiber, EH_{11} intersects TE_{01} at a single degeneracy point (here, at $\lambda = 1.698\mu\text{m}$)—the vicinity of this point must therefore be excluded from the usable bandwidth. From the scaling laws of Eqs. (4,5), however, we see that $HE_{1\ell}$ modes may have smaller $\Delta\beta$ for large R—for the present structure, the HE_{11} and HE_{12} modes make a significant contribution (often 50%) to the bend losses for many wavelengths.

We compute the minimum bending radius $R_{0.1\%}$ for which the worst-case scattered power from Eq. (46) is 0.1%. As shown in the appendix, this is ostensibly independent of the number of turns—the scattered power of Eq. (46) simply oscillates with bending distance. There are additional loss mechanisms for large numbers of turns that we consider below, however. In this computation, we include the $EH_{1\ell}$ and $HE_{1\ell}$ modes for $\ell = 1, 2, 3$; the contribution of other modes is negligible. The results are plotted in Fig. 12. To find the losses for a different bend radius R_b, one would then scale 0.1% by $(R_{0.1\%}/R_b)^2$ (although this fails as the losses approach 100% and perturbation theory is no longer valid). Furthermore, given the $\Delta\beta$ scaling from Eq. (5) and the fact that the integrand of Eq. (12) yields an additional factor of R, we find that:

$$\text{minimum bend } R_b \text{ for 0.1\% losses, } R_{0.1\%} \sim R^2. \tag{15}$$

For large R, however, if coupling to HE modes with $\Delta\beta \sim 1/R^2$ begins to dominate, one has instead $R_{0.1\%} \sim R^3$.

7.2.1   *Long-distance bends: effects of lossy modes*

Matters become more complex when the bend continues for a long distance, where one must take into account the lossiness of the modes. (Random variations in the bend could also be considered, by the techniques of Sec. 8.3.) In the derivation of Eq. (46), parasitic waves scattered at earlier positions interfere with waves scattered at later positions due to the phase mismatch $\Delta\beta$. If the parasitic mode is lossy, however, the wave from the earlier position may have decayed away before it can interfere. Qualitatively, then, one
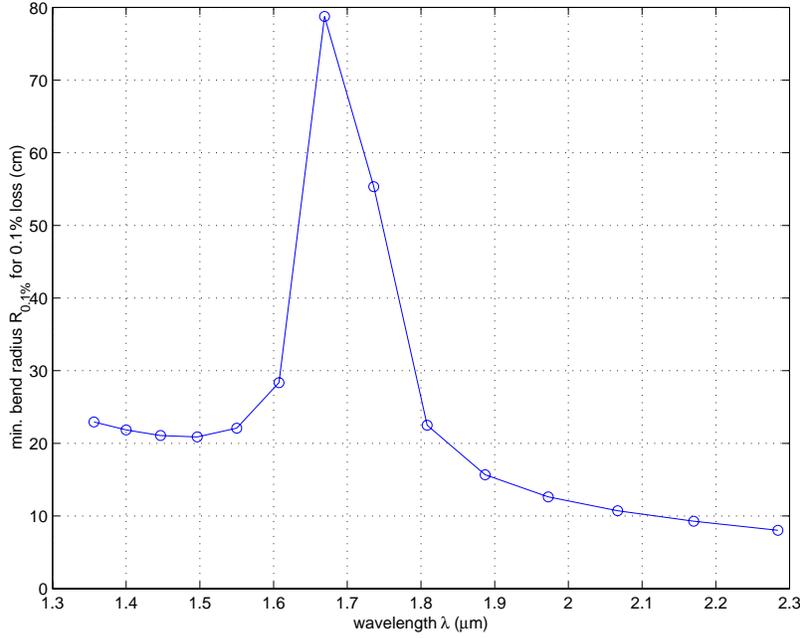
Fig. 12. Minimum bending radius $R_{0.1\%}$ to achieve 0.1% worst-case scattering losses for the TE_{01} mode in the OmniGuide fiber of Fig. 4. Conversely, the losses for a given bending radius R_b are $0.1\% \cdot (R_{0.1\%}/R_b)^2$. The sharp peak (actually a divergence) in $R_{0.1\%}$ is due to the point of degeneracy between TE_{01} and EH_{11}.

expects that the scattering will follow Eq. (46) for roughly a decay length of the mode, and will then "restart" once the original parasitic modes have decayed. Quantatitively, we estimate the effective decay rate of the "hybridized" curved-waveguide eigenmode by computing its new *complex* $\widetilde{\beta}$ from Eq. (44)—simply substituting the complex $\beta_n + i\alpha_n/2$ into the equation, where α_n is the power decay rate of $|n\rangle$. For $\Delta\alpha \ll \Delta\beta$, this yields:

$$\Delta\alpha_n^{(2)} \cong \sum_{n' \neq n} \frac{\left|\left\langle n' \left| \Delta\hat{A} \right| n \right\rangle\right|^2}{\Delta\beta_{n'n}^2} (\alpha_{n'} - \alpha_n), \qquad (16)$$

the lowest-order shift in the decay rate.[13] This equation corresponds to taking the mean scattering losses from Eq. (46) once every $2/\Delta\alpha_{n'n}$ decay length. (If the modes both decay at the same rate, the field powers simply scale with distance and the interference proceeds as before.) When $|n\rangle$ is TE_{01}, we will have $\alpha_{n'} \gg \alpha_n$ as in Figs. 7 and 9.

For example, at $\lambda = 1.55\mu$m in our case of the $R = 30a$ OmniGuide fiber with 17 layers, the radiation decay length $2/\alpha$ of EH_{11} is 60m from Fig. 7, with a bend radius $R_{0.1\%}$ of 20cm for 0.1% losses. Then, to induce a decay rate $\Delta\alpha^{(2)}$ in TE_{01} of only 0.01 dB/km, one needs the average bending radius to be $\gtrsim$ 40cm (neglecting the coupling to modes besides EH_{11}).[14] If this were too large, or if EH_{11} were more lossy (say, due to a smaller bandgap), then one could simply add more periods to the Bragg mirrors until the EH_{11} radiation losses were sufficiently low.

---

[13]The fact that this decay rate is second-order in the perturbation $1/R_b$ was also found in hollow metallic waveguides [16, 17, 37], by explicitly solving for the eigen-field correction in the curved waveguide.

[14]In an undersea cable, the fiber spirals continuously within a central core, to prevent the fiber from bearing any of the cable tension—a typical radius of bending curvature would be around 50cm (corresponding to 5% fiber slack and a 5cm core radius).

8 Elliptical and Uniform-Scaling Perturbations

In this section, we apply perturbation theory to treat elliptical and uniform-scaling perturbations of the fiber cross section, and develop a general form for the perturbation operator. To begin with, we consider the effect of a constant ellipticity/scaling along the length of the fiber. For doubly-degenerate linearly-polarized $m = 1$ modes such as EH_{11}, our formulation provides a quantitative way to understand ellipticity-induced birefringence and polarization mode dispersion (PMD). Here, however, in the case of $m = 0$ singlet modes (such as TE_{01}) in an OmniGuide fiber, the main effect of ellipticity is to increase radiation losses by coupling to other, much lossier, modes. Our expressions apply even for large index contrasts within the fiber, and the validity of the perturbation theory depends only on the amount of ellipticity/scaling.

There has been much previous research on estimating such quantities as the local birefringence induced by perturbations in the fiber profile, and such analyses can be found in many standard textbooks [23, 38]. Most such treatments, however, are geared toward understanding low-contrast, weakly guiding systems such as the ubiquitous silica fiber, and are not directly applicable to high-contrast systems such as OmniGuide fibers, as well as *e.g.* photonic-crystal fibers or lithographic integrated waveguides. While several approaches have been suggested for the perturbative treatment of such high index-contrast systems [23, 39–43] there is still no consensus on the best form for such an analysis.

Ellipticity and scaling correspond to moving dielectric-interface boundaries, and one way to analyze this would ostensibly be to find the change $\Delta\varepsilon$ and substitute it into the general formula of Eq. (48). However, as discussed in Sec. 8.2 and in analyzed in detail by [44], this formulation yields incorrect results (compared to exact calculations) for large contrasts $\Delta\varepsilon$, due to the changing boundary conditions on the fields. Instead, we employ a different approach that maintains the field boundary conditions at the interfaces: we rescale the coordinates to $x_s = x(1 + \delta_x)$, $y_s = y(1 + \delta_y)$ and compute the modified $\hat{A}$ of Eq. (38). In particular, we focus on two cases: a uniform scaling $\delta_x = \delta_y$, and an elliptical scaling $\delta_x = -\delta_y$. This change of coordinates alters the curl operations and induces a perturbation $\Delta\hat{A}$. Then, as before, we use z-independent perturbation theory to compute the corrected β of the perturbed eigenmodes, the birefringence, and the induced losses. To treat scaling or ellipticity that vary along the propagation direction, z-dependent perturbation theory can be employed to calculate the coupling/scattering. We believe that this is the first general perturbative treatment for fiber ellipticity that is capable of handling large index contrasts.

8.1 *Elliptical perturbations*

We first consider the case of a uniform elliptical perturbation via the rescaling $\delta \equiv \delta_x = -\delta_y$, and define $\eta \equiv \delta/(1+\delta) \cong \delta$. In this case, we find after some cumbersome algebra [44] that the perturbation matrix elements take the following form in a cylindrical fiber:

$$\left\langle n'; m' \left| \Delta\hat{A} \right| n; m \right\rangle = \left\langle \begin{array}{c} E_r' \\ E_\varphi' \\ H_r' \\ H_\varphi' \end{array} \right| \frac{\omega}{c}\eta \left(\begin{array}{cccc} -\varepsilon & \pm i\varepsilon & & \\ \pm i\varepsilon & \varepsilon & & \\ & & -\mu & \pm i\mu \\ & & \pm i\mu & \mu \end{array} \right) \left| \begin{array}{c} E_r \\ E_\varphi \\ H_r \\ H_\varphi \end{array} \right\rangle \delta_{m',m\mp 2}, \quad (17)$$

where we have expressed the transverse fields in their cylindrical components, and the final Kronecker delta expresses a selection rule that only $|\Delta m| = 2$ modes can directly couple under this form of perturbation.

In the case of a singlet $m = 0$ mode, *e.g.* the TE_{01} operating mode of the OmniGuide fiber, the introduction of such ellipticity leads to only a second-order shift in the real

part of β from Eq. (44), as well as increased losses from Eq. (16). Because a single mode can never be split into two modes, the birefringence and consequently the PMD for any $m = 0$ mode is zero.

Although the scaling of Eq. (17) is non-obvious, an empirically correct result is obtained here by postulating that an expression like Eq. (48) could be found even for large index contrasts: *i.e.* that the matrix element scales as the field integral over the perturbation $\Delta\varepsilon$'s area. This area scales as $\delta \cdot R$, while the normalized field-amplitude $\left|\vec{E}\right|$ inside the perturbation scales as $1/R^2$ for $\mathrm{TE}_{0\ell}$ from Eq. (2). On the other hand, this field amplitude is $\sim 1/R$ for $m \neq 0$ modes. Thus, the following scaling is obtained:

$$\left\langle \mathrm{TE}_{0\ell} \left| \Delta\hat{A} \right| m = \pm 2 \right\rangle \quad \sim \quad \frac{\delta}{R^2}. \tag{18}$$

8.1.1 *Scaling relations and increased losses for $TE_{0\ell}$ modes*

Given the matrix element of Eq. (17) and the scaling relation of Eq. (18), we can find the form of the shift in the complex propagation constant $\widetilde{\beta}$ and the attenuation rate α via Eqs. (16, 44). The latter equations are inversely proportional to the mode separation $\Delta\beta$, which scales as $1/R^2$ from Eq. (4). Thus:

$$\Re\left[\Delta\widetilde{\beta}^{(2)}\right] \sim \frac{\delta^2}{R^2}. \tag{19}$$

We consider the imaginary part (the attenuation rate) separately via Eq. (16). There, one divides by $\Delta\beta^2$; on the other hand, we showed that the radiative/dissipative decay rates α of the $m \neq 0$ modes scale as $1/R$, and thus:

$$\Delta\alpha^{(2)} = 2\Im\left[\Delta\widetilde{\beta}^{(2)}\right] \sim \frac{\delta^2}{R}. \tag{20}$$

These two scaling relations are verified in Fig. 13, where we plot the real and imaginary parts of $\Delta\widetilde{\beta}^{(2)}$ as a function of core radius R for the OmniGuide TE_{01} mode with 1% ellipticity. The large additional loss induced by the ellipticity comes from the coupling to mixed-polarization modes that have large radiation losses, due to the smaller TM band gap—this can be ameliorated, however, by increasing the number of cladding layers, as discussed below.

Another important result for the radiation loss of the elliptically perturbed TE_{01} mode is its scaling with respect to the number of layers in the omnidirectional mirror. This scaling is depicted in Fig. 14. For comparison, we also show the radiation losses of the unperturbed TE_{01} and $\mathrm{HE}_{21}/\mathrm{EH}_{21}$ modes, where the latter contribute the dominant coupling terms in Eq. (16) for $\Delta\alpha^{(2)}$. As the number of layers in the mirror increase, the radiation losses of HE_{21} and other $m = 2$ modes become exponentially greater than the TE_{01} losses, due to the smaller TM band gap. Thus, for a large number of layers, TE_{01} losses are expected to be totally dominated by the losses via ellipticity-coupling to the $m = 2$ modes, and moreover will have the same slope as the α of the TM modes.

8.2 *Uniform-scaling perturbations*

By the same methods, we can find the analogous perturbation matrix elements in the case of uniform rescaling of the fiber, $\delta \equiv \delta_x = \delta_y$ and $\eta \equiv \delta/(1 + \delta) \cong \delta$. Although we do not use this result directly here, uniform scaling has the advantage of being easily checked against an exact transfer-matrix computation. We have done this, computing $\partial\beta/\partial\eta$ and $\partial^2\beta/\partial\eta^2$ via Eqs. (43,44), and found that our perturbation theory yields the
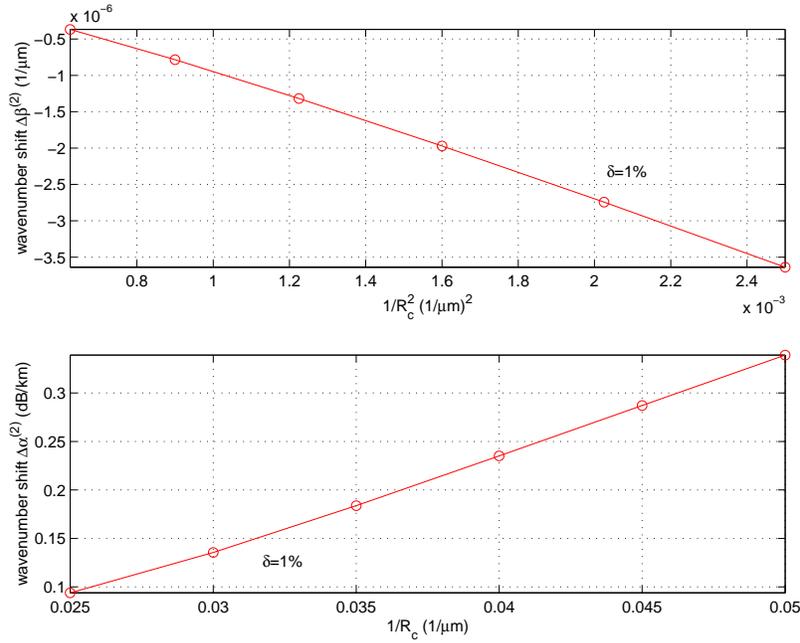
Fig. 13. Scaling of the ellipticity-induced phase shift $\Re[\Delta\widetilde{\beta}^{(2)}]$ and loss $\Delta\alpha^{(2)}$ for the OmniGuide-fiber TE_{01} mode at $\lambda = 1.55\mu m$ as a function of the core radius R, varying from 20–80a. The abscissa is the expected scaling form of $1/R^2$ and $1/R$, respectively. The amount of ellipticity is $\delta = 1\%$ and the cladding has 17 layers.
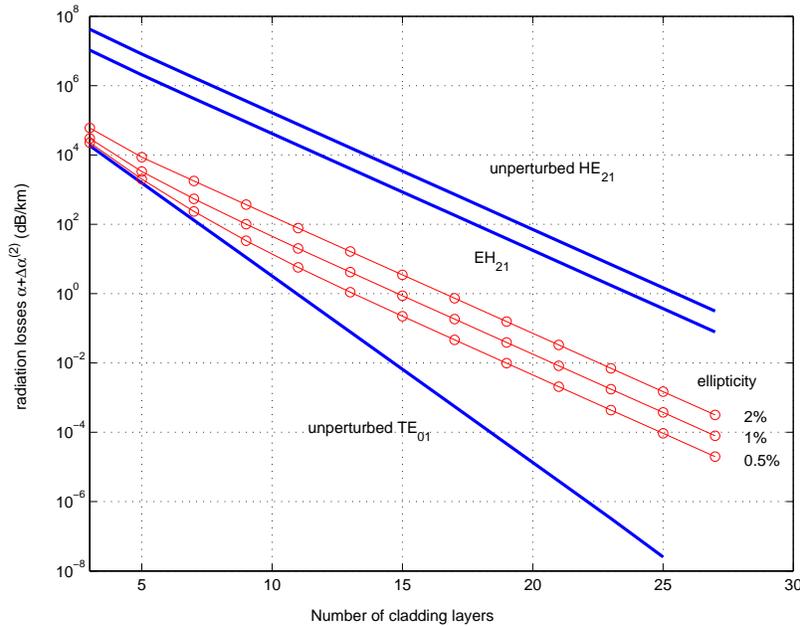

Fig. 14. The estimated radiative loss $\alpha + \Delta\alpha^{(2)}$ of the TE_{01} mode at $\lambda = 1.55\mu m$ for the OmniGuide fiber of Fig. 4 with an elliptical perturbation, plotted versus the number of cladding layers for three ellipticities: $\delta = 0.5\%, 1\%, 2\%$. Red circles indictate the losses for the perturbed fibers, while solid blue lines above and below are the losses of the unperturbed HE_{21} and TE_{01} modes, respectively. As the number of layers increases, the losses become dominated by coupling to HE_{21}, due to the weaker band gap for TM polarizations.

correct results for all modes. In contrast, using Eq. (48) to compute $\partial\beta/\partial\eta$ is found to produce the correct results only for pure TE $m = 0$ modes—the reason for this is that the changing discontinuity condition on E_r makes the unperturbed modes a poor basis for TM and mixed-polarization modes, causing significant errors in high index-contrast systems [44].

8.3 *Nonuniform stochastic elliptical perturbations*

Elliptical deformations of an OmniGuide fiber can cause two sorts of losses. Above, we estimated the losses that come from the ellipticity *per se*, due to the induced mode mixing, assuming that TE_{01} was adiabatically transformed into the analogous elliptical-fiber mode. As a fiber is drawn, however, there will be stochastic variations in the ellipticity along the fiber length, and this will create scattering losses in which power is transferred non-adiabatically from TE_{01} to other modes. Assuming that there is no systematic ellipticity, one can derive coupled-power equations averaged over an ensemble of possible stochastic ellipticity realizations. These equations for the transfer of power between modes take the form of a well known master equation [45]. Defining P_n as a relative power in the n-th mode (with decay rate α_n), one has:

$$\frac{\partial P_n}{\partial z} = -\alpha_n P_n + \sum_m M_{nm}(P_m - P_n), \tag{21}$$

where the coupling (transition probability) M_{nm} is defined as follows. First, we separate the perturbation $\Delta\hat{A}$ of Eq. (17) from the ellipticity δ by $\Delta\hat{A} \equiv \delta \cdot \Delta\hat{a}$, and suppose that the ellipticity $\delta(z)$ is a stochastic function with zero mean and an autocorrelation $C(z) \equiv \langle\delta(\zeta)\delta(\zeta - z)\rangle$. Defining the Fourier transform $\Xi(\kappa) \equiv \int C(z)e^{-i\kappa z}dz$, we arrive at [45] $M_{nm} \equiv |\langle n|\Delta\hat{a}|m\rangle|^2\Xi(\beta_n - \beta_m)$. One must choose a form for the autocorrelation function $C(z)$, and here we assume that it is a Gaussian with rms ellipticity δ_0 and a correlation length $L_c(\delta_0)$: $C(z) = \delta_0^2 e^{-[z/L_c(\delta_0)]^2}$. For stochastic ellipticity from fiber drawing, a typical $\delta_0 \sim 1\%$ [46], and it is likely that $L_c \gtrsim 10cm$.

The linear equations of Eq.(21) can be solved by finding their eigenvectors $\vec{p}_j$ and eigenvalues $-\widetilde{\alpha}_j$, where the effective decay rates $\widetilde{\alpha}_j$ are real as long as the autocorrelation $C(z)$ is real-symmetric, and they can also be shown to be non-negative [45]. These $\widetilde{\alpha}_j$ are the effective decay rates, and after a long distance the decay will be dominated by the smallest eigenvalue $\widetilde{\alpha}_0$ and its corresponding equilibrium power distribution $\vec{p}_0$. In the case of the OmniGuide fiber, elliptical perturbations of Eq. (17) couple the TE_{01} mode predominantly to HE_{21}. Using these two modes and Eq.(21), we compute the effective loss rate $\widetilde{\alpha}_0$ as a function of L_c for the OmniGuide fiber with $\delta_0 = 1\%$ at $\lambda = 1.55\mu m$.[15] The results, presented in Fig. 15, show that as long as $L_c \gtrsim 1.6mm$, the scattering into the the lossier HE_{21}/EH_{21} modes yields TE_{01} losses $\widetilde{\alpha}_0 < 0.01$ dB/km. In the insert, we plot the relative power in the modes as a function of L_c. For $L_c \gtrsim 1.6mm \sim 1/\Delta\beta$, the fractional power in the parasitic modes is less than 10^{-4}.

9 Uncorrelated Roughness Losses

Another potential source of losses in any fiber is interface roughness and, since such effects worsen with increasing index contrast, they may be a practical concern in OmniGuide fibers. In this section, we make an order-of-magnitude estimate of roughness losses in an OmniGuide fiber, assuming *uncorrelated* small scatterers on the core/cladding interface. Fortunately, we find that the near-node in the electric field at the interface has the effect of greatly suppressing such roughness effects.

---

[15]We have also solved the equations with 16 modes and found that the main conclusions are the same as in the case of two-mode coupling, with merely a more complicated curve shape.
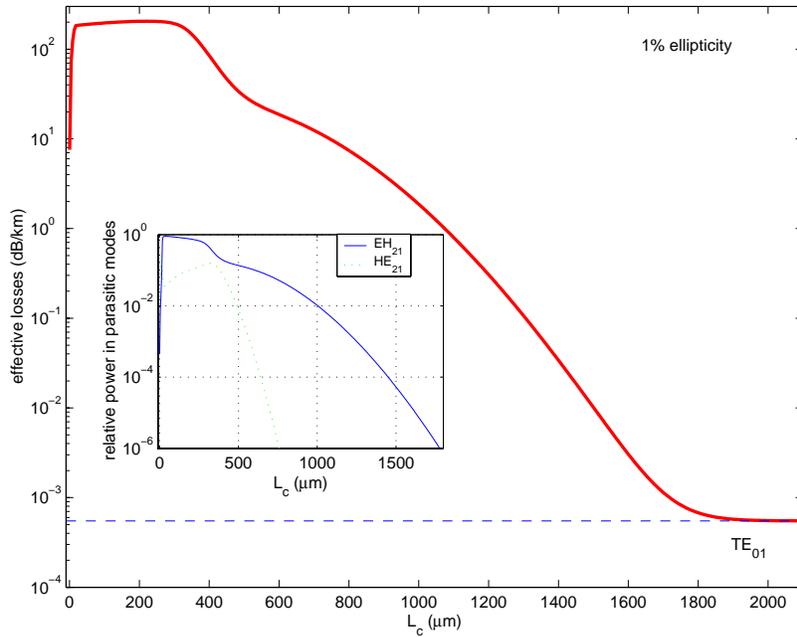
Fig. 15. Enhanced loss of the TE_{01} mode at $\lambda = 1.55\mu$m from randomly-varying ellipticity with rms $\delta_0 = 1\%$, as a function of the ellipticity correlation length L_c, due to coupling with the HE_{21} and EH_{21} modes. The inset shows the fractional scattered power in the parasitic HE_{21}/EH_{21} modes as a function of L_c. If the correlation length exceeds ~ 1.6mm, the induced losses become smaller than 0.01 dB/km and the fractional parasitic power is less than 10^{-4}.

Suppose that we have a scatterer with volume V_s and a $\Delta\varepsilon$ given by the core/cladding contrast. Since it is small, we take $\vec{E}$ to be roughly constant inside V_s, in which case the scatterer can be treated by the volume-current method [47] as a radiating dipole with moment $\vec{p} = \Delta\varepsilon\vec{E}V_s$.[16] Instead of exactly computing the lost radiation, we make several order-of-magnitude approximations. First, we assume that all radiated power is lost, since only negligible fraction should re-radiate into TE_{01} compared to all the other modes ($\Delta\beta$ and Δm are irrelevant for a point-like perturbation). Second, since the core is much larger than the wavelength, we neglect its finite size and consider a dipole radiating on a planar interface between semi-infinite regions. Third, we neglect the effect of the omnidirectional mirrors on one side of the dipole; generally, these are expected to reduce the radiated field, so this is a conservative approximation. Thus, in the end, we treat V_s as simply a dipole radiating in vacuum, with scattered power [38]:

$$P_s = \frac{c^2\sqrt{\frac{\mu_0}{\varepsilon_0}}}{12\pi}\left(\frac{\omega}{c}\right)^4|\vec{p}|^2 = \frac{\omega^4}{12\pi}\left|\Delta\varepsilon\vec{E}V_s\right|^2, \tag{22}$$

in dimensionless units ($c = \mu_0 = \varepsilon_0 = 1$) for simplicity.

This is the approximate power radiated by a single scatterer. For multiple scatterers distributed along the waveguide in an uncorrelated fashion, so that their radiation is *incoherent*, one can simply add the power radiated from each one. If the scatterers have density σ_s (scatterers per interface area) then the power radiated per length is $P_s \cdot 2\pi R\sigma_s$. To convert this into a power-attenuation rate α, we divide it by the forward-propagating

---

[16]This is an approximation for large $\Delta\varepsilon$; the correct moment is generally less—see *e.g.* the induced dipole moment of a spherical scatterer in [38].
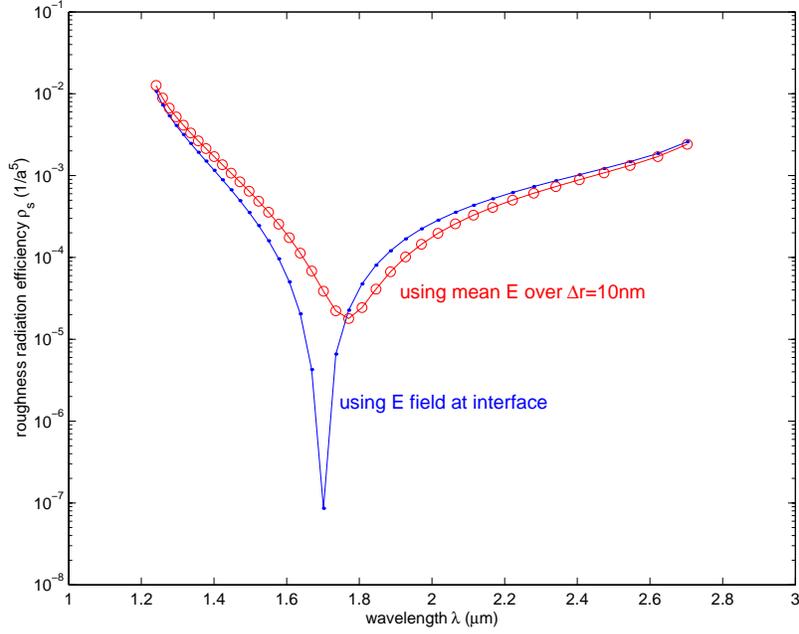
Fig. 16. Roughness radiation efficiency ρ_s, as defined by Eq. (24) for the TE$_{01}$ mode of the OmniGuide fiber of Fig. 4, based on the $|\vec{E}|^2$ at the core/cladding interface (blue dots) or averaged over a 10nm interval (red circles). Approximate roughness losses are computed by multiplying ρ_s with a dimensionful quantity s that is dependent on the scatterer quantity; *e.g.* $s = 0.03$ dB/km for one 10nm scatterer every $10\mu m^2$.

power $P = \langle n|\hat{B}|n\rangle /4 = 1/4$ (*c.f.* Eq. (42)) in our normalized field units:

$$\alpha = \frac{P_s \cdot 2\pi R \sigma_s}{P} = \left(\frac{\omega^4}{12\pi} \left| \Delta\varepsilon\vec{E} \right|^2 \cdot 2\pi R \cdot 4 \right) \cdot \sigma_s V_s^2, \tag{23}$$

where we have separated out the terms that are independent of our assumptions about the scatterer dimensions. Together, the parenthesized terms have units of $1/\text{length}^5$ in our units, and we can compute them as a "dimensionless" radiation "efficiency" factor ρ_s in our units of $1/a^5$:

$$\rho_s \equiv \frac{2\omega^4 R}{3} \left| \Delta\varepsilon\vec{E} \right|^2, \tag{24}$$

and from that compute $\alpha = \rho_s \cdot s$, where s is the dimensionful measure of the scatterer quantity:

$$s \equiv \frac{\sigma_s V_s^2}{a^5} \cdot \frac{10}{\ln 10}, \tag{25}$$

with a $10/\ln 10$ factor to convert to dB units (*e.g.* dB/km). If we take the scatterer size to be $V_s \cong (10\text{nm})^3$ and $\sigma_s \cong 0.1/\mu m^2$, this gives $s \cong 0.03$ dB/km for the a of the OmniGuide fiber. In Fig. 16, we plot ρ_s vs. λ for our fiber, taking $\vec{E}$ as the field at the interface. The plot indicates a sharp dip towards $\rho_s = 0$, due to the point where the node in the field lies directly on the interface—this feature is unphysical, since it indicates a breakdown of our assumption of constant $\vec{E}$ in the scatterer. For comparison, we also plot ρ_s where $|\vec{E}|^2$ is averaged over $\Delta r = 10$nm. In either case, we see that $\rho_s < 10^{-3}$ over a wide bandwidth, providing a comfortable margin in both the scatterer parameters V_s and σ_s as well as our earlier approximations. In general, $|\vec{E}|^2$ at the interface goes

like $1/R^4$ from Eq. (2), so the uncorrellated roughness losses are expected to scale as $1/R^3$ (just like the radiation-leakage and absorption losses).

10   Scaling Laws with Index Contrast

Although the computations in this paper assumed an index contrast of 4.6/1.6, the same qualitative results hold for a wide range of indices as long as the confinement remains strong. The index contrast manifests itself in the decay rate of the field into the cladding, which determines the characteristic penetration depth d_p, and the analogy with the metallic waveguide remains valid when $d_p \ll R$. Below, we derive scaling relations to predict how the OmniGuide-fiber properties will vary with the cladding indices (assuming $d_p \ll R$).

In particular, with each bilayer of cladding, the fields decrease by some attenuation factor $\kappa(\omega, \beta)$. For modes nearly on the $\omega = c\beta$ light line, using "quarter-wave" bilayers given by Eq. (1), and defining $\widetilde{n} \equiv \sqrt{n^2 - 1}$, the mid-gap κ for TE/TM fields is [3, 22]:

$$\kappa_{\text{te}} \cong \frac{\widetilde{n}_{\text{lo}}}{\widetilde{n}_{\text{hi}}}, \tag{26}$$

$$\kappa_{\text{tm}} \cong \frac{n_{\text{lo}}^2 \widetilde{n}_{\text{hi}}}{n_{\text{hi}}^2 \widetilde{n}_{\text{lo}}} > \kappa_{\text{te}}. \tag{27}$$

The penetration depth d_p of $|\vec{E}|^2$ is then proportional to $a/(1 - \kappa^2)$. From Sec. 3, the TE$_{0\ell}$ cladding $|\vec{E}| \sim d_{\text{hi}}/R^2 = f_{\text{hi}} a/R^2$, where $f_{\text{hi}} \equiv d_{\text{hi}}/a = \widetilde{n}_{\text{lo}}/(\widetilde{n}_{\text{lo}} + \widetilde{n}_{\text{hi}})$ from Eq. (1). We can then generalize Eq. (3) to:

$$\text{fraction of } \int |\vec{E}|^2 \text{ in cladding for TE}_{0\ell} \sim \frac{f_{\text{hi}}^2}{(1 - \kappa_{\text{te}}^2)} \left(\frac{a}{R}\right)^3. \tag{28}$$

The scaling of absorption loss is the same, except that from Sec. 6.1 it also proportional to n, whose average is $\bar{n} \equiv (n_{\text{hi}} - n_{\text{lo}})f_{\text{hi}} + n_{\text{lo}}$. Thus,

$$\text{TE}_{0\ell} \text{ cladding absorption} \sim \frac{\bar{n} f_{\text{hi}}^2}{(1 - \kappa_{\text{te}}^2)} \left(\frac{a}{R}\right)^3. \tag{29}$$

One can similarly find the scaling of nonlinearities (whose integrand is $n|\vec{E}|^4$):

$$\text{TE}_{0\ell} \text{ cladding nonlinearity } \frac{\gamma}{\gamma_0} \sim \frac{\bar{n} f_{\text{hi}}^4}{(1 - \kappa_{\text{te}}^4)} \left(\frac{a}{R}\right)^5. \tag{30}$$

We have verified that these scalings are accurate over a wide range of index contrasts, and corresponding relations can also be found for the other quantities computed in this paper.

The number of cladding layers required to achieve a given radiation leakage rate for TE or TM modes scales inversely with $\log(1/\kappa_{\text{te}})$ or $\log(1/\kappa_{\text{tm}})$, respectively. So, for example, if one used indices of 1.459/1.450 (doped silica) [8, 9], ~ 2000 cladding layers would be required to achieve the same TE radiation-leakage rates as in Fig. 7.

The bandwidth also varies with index contrast. One is limited by the size of the TM gap along the light line (due to coupling such as in Sec. 8.1.1), and the fractional size of the TM gap on $\omega = c\beta$ for our quarter-wave stack is [22]:

$$\frac{\Delta\omega_{\text{tm}}}{\omega_0} = \frac{4}{\pi} \sin^{-1} \left(\frac{n_{\text{hi}}^2 \widetilde{n}_{\text{lo}} - n_{\text{lo}}^2 \widetilde{n}_{\text{hi}}}{n_{\text{hi}}^2 \widetilde{n}_{\text{lo}} + n_{\text{lo}}^2 \widetilde{n}_{\text{hi}}}\right), \tag{31}$$

where ω_0 is the mid-gap frequency:

$$\omega_0 = \frac{\widetilde{n}_{\mathrm{lo}} + \widetilde{n}_{\mathrm{hi}}}{4\widetilde{n}_{\mathrm{lo}}\widetilde{n}_{\mathrm{hi}}} \cdot \frac{2\pi c}{a}. \tag{32}$$

The periodicity a changes with index as well, assuming a fixed vacuum λ. If λ is chosen to be near ω_0, and $\nu_0 \equiv \omega_0 a/(2\pi c)$, then $a \sim \lambda\nu_0$.

11 Concluding Remarks

We have presented the propagation characteristics of the lowest-loss TE_{01} mode in an example OmniGuide fiber with a large core radius $R = 30a$. Although it is impossible to consider all possible imperfections in such a fiber, we have studied radiation leakage, material absorption, nonlinearities, bends, acircularity, and roughness, and have shown that all of these are within acceptable bounds. Indeed, such properties as material absorption and roughness are suppressed by four or more orders of magnitude, holding forth the promise of optical fibers with substantially lower losses and negligible nonlinearities compared to conventional silica fibers—even when highly lossy and nonlinear materials are used for the multilayer cladding. (The same properties open the possibility of fibers for currently inaccessible wavelengths.) Almost all OmniGuide fiber properties are dominated by the geometry of the core, and for a wide range of R follow generalized scaling relations that we have derived, as summarized in Table 1. Even though such a large-core OmniGuide fiber is ostensibly highly multi-mode, the higher losses of the other modes creates a modal-filtering effect that allows the fiber to operate in a single-mode fashion as long as the differential losses are greater than the rate of coupling from imperfections. In this respect, and in many others, such a fiber is analogous to the hollow metallic waveguides that have been extensively studied in the microwave regime. In future publications, we will consider many of these issues in greater detail, as well as other topics such as input/output coupling and dispersion tailoring.

Many of our results were developed from a general perturbation theory, derived from an abstract eigenproblem formulation, that can be applied to arbitrary waveguiding systems. This perturbation theory is summarized in the following appendix, whereas the specific forms of the perturbation operator for particular imperfections were presented in the preceding sections.

quantity	scaling
typical mode separation $\Delta\beta$	$1/R^2$, or $1/R$ with EH_{11}
group-velocity dispersion D	$1/R^2$
leakage, absorption, and roughness losses	$1/R^3$
cladding nonlinearity suppression	$1/R^5$
minimum bend radius $R_{0.1\%}$ for 0.1% bend losses	$R^2 \cdots R^3$
ellipticity-δ losses from mode mixing	δ^2/R

Table 1. Scaling relations with core radius R for TE_{01} in OmniGuide fibers.

Appendix: Waveguide Perturbation Theory

Having computed the exact eigenmodes of a perfect OmniGuide fiber via the transfer matrix method, we then considered the problem of various imperfections and perturbations to this idealized situation, such as absorption, nonlinearities, bending, ellipticity, and so on. In principle, one could compute the exact solutions under these conuiditions, but since the effects are small, they can be more efficiently estimated via perturbation

theory. We outline the development of such a perturbation theory in this appendix, and a later publication will consider the matter in greater detail [48].

Perturbation theory has been developed in many forms for Maxwell's equations. Here, we derive it by first expressing Maxwell's equations in waveguides as a (vectorial) generalized eigenproblem, and then appropriating the perturbation theory from the standard abstract-algebraic formulation developed for quantum mechanics [49]. Particular waveguide perturbations are then simply a matter of finding the change in the eigen-operator induced by the perturbation. This approach to perturbation theory has the advantage of separating the details of Maxwell's equations and the particular system from the generic eigenproblem algebra, but has not been widely used for the full-vector electromagnetic waveguide problem. Earlier work has preferred other methods, which in most cases yield equivalent results to our unified approach, but we have also found some novel generalizations and formulations.

In the following section, we use the Dirac notation of abstract state *kets* $|\psi\rangle$ and linear operators $\hat{A}$, where the state in this case represents the electromagnetic fields. The inner product $\langle\phi|\psi\rangle$ is defined below.

The Maxwell Waveguide Eigenproblem

Here, we derive a general, abstract formulation for the propagation equation of electromagnetic states in a waveguide along the $\hat{z}$ direction. Furthermore, we show that the modes of the waveguide satisfy a Hermitian generalized eigenproblem in β, which will then yield orthogonality relations, perturbation theory, and other results. An alternative eigenproblem in ω is described in [1], and another eigenproblem formulation for use in plasma physics was presented in [50]

Consider the source-free Maxwell's equations for fields with a definite-frequency time-dependence $e^{-i\omega t}$. In this case, the $\vec{E}$ and $\vec{B}$ fields can be cast purely in terms of their transverse ($\hat{x}$ and $\hat{y}$) components $\vec{E}_t$ and $\vec{B}_t$ [23, 38], since:

$$H_z = \frac{-ic}{\omega\mu}\vec{\nabla}_t \times \vec{E}_t, \tag{33}$$

$$E_z = \frac{ic}{\omega\varepsilon}\vec{\nabla}_t \times \vec{H}_t \tag{34}$$

With this substitution, and moving all of the z derivatives to one side in Maxwell's equations, the field equations take on the form:

$$\hat{A}|\psi\rangle = -i\frac{\partial}{\partial z}\hat{B}|\psi\rangle, \tag{35}$$

where we define $\hat{A}$, $\hat{B}$, and $|\psi\rangle$ below. Eq. (35) plays the role of Schrödinger's equation from quantum mechanics, with z taking the place of time. $|\psi\rangle$ is (abstractly) the electromagnetic field pattern as a function of z, and (concretely), in this case, is represented by the 4-component column vector:

$$|\psi\rangle \equiv \left(\begin{array}{c} \vec{E}_t(z) \\ \vec{H}_t(z) \end{array} \right), \tag{36}$$

where we define the inner product of two states $|\psi\rangle$ and $|\psi'\rangle$ by:

$$\langle\psi|\psi'\rangle \equiv \int \vec{E}_t^* \cdot \vec{E}_t' + \vec{H}_t^* \cdot \vec{H}_t', \tag{37}$$

and the integral is over the waveguide cross-section at a given z. $\hat{A}$ and $\hat{B}$ are the *Hermitian* operators (under this inner product):

$$\hat{A} \equiv \begin{pmatrix} \omega\varepsilon/c - \frac{c}{\omega}\vec{\nabla}_t \times \frac{1}{\mu}\vec{\nabla}_t \times & 0 \\ 0 & \omega\mu/c - \frac{c}{\omega}\vec{\nabla}_t \times \frac{1}{\varepsilon}\vec{\nabla}_t \times \end{pmatrix}, \tag{38}$$

$$\hat{B} \equiv \begin{pmatrix} 0 & -\hat{z}\times \\ \hat{z}\times & 0 \end{pmatrix} = \begin{pmatrix} & & & 1 \\ & & -1 & \\ & -1 & & \\ 1 & & & \end{pmatrix} = \hat{B}^{-1}. \tag{39}$$

Note that $\hat{A}$ is positive-definite (for $\omega > 0$), but $\hat{B}$ is not; more on this below. Also, $\hat{A}$ is Hermitian if ε is purely real—in physical systems, ε has a small imaginary part corresponding to material absorption, but we add this feature *a posteriori* in Sec. 6.1 via perturbation theory.

To start with, we consider the ideal case where the waveguide is uniform along z, in which case the Bloch-Floquet theorem [51] implies that the states of the system can be chosen with a z-dependence of the form $e^{i\beta z}$ for some wavenumber β. These are the eigenmodes of the waveguide, *i.e.* the "normal modes" [23]:

$$e^{i(\beta z - \omega t)} |\psi\rangle. \tag{40}$$

Substituted into Eq. (35), they satisfy the Hermitian generalized eigenproblem:

$$\hat{A} |\psi\rangle = \beta\hat{B} |\psi\rangle. \tag{41}$$

These states must satisfy the usual properties of Hermitian eigenproblems, albeit somewhat modified from quantum mechanics by the presence of a non-positive-definite $\hat{B}$:

- The eigenvalues β are real as long as $\langle\psi|\hat{B}|\psi\rangle \neq 0$. (Because $\hat{B}$ is not positive-definite, this is not always true, leading to evanescent modes with complex or imaginary β.)

- Orthogonality: for two eigenstates $|\psi\rangle$ and $|\psi'\rangle$ with eigenvalues β and β' such that $\beta^* \neq \beta'$, $\langle\psi|\hat{B}|\psi'\rangle = 0$.

- The eigenstates generally form a *complete basis* for the system.

- For localized modes (*e.g.* guided modes of a waveguide), the eigenvalues are a discrete sequence β_n with eigenstates $|n\rangle$.

The orthonormality relation, expressed explicitly in terms of the transverse fields, becomes:

$$\left\langle\psi\left|\hat{B}\right|\psi'\right\rangle = \hat{z} \cdot \int \vec{E}_t^* \times \vec{H}_t' + \vec{E}_t' \times \vec{H}_t^*, \tag{42}$$

which is proportional to the forward-propagating power for $\langle\psi|\hat{B}|\psi\rangle$. The fact that eigenmodes are orthogonal under this metric has previously been derived from the Lorentz reciprocity theorem for electromagnetism [23], whereas here it follows automatically from the general properties of Hermitian eigenproblems.

In this paper, we focus primarily on the propagating (real β), guided (discrete β) modes of the waveguide. We normalize them so that $\langle n|\hat{B}|n\rangle = 1$. When one expands a field in the eigenstates, in principle the continuum and evanescent modes are required as well, but we shall show that in the cases of interest here, only a few guided modes are needed for acceptable accuracy.

Perturbation Theory

Given a Hermitian eigenproblem, we can now directly employ the perturbation-theory formulations derived for quantum mechanics [49] in order to find the effects of a small perturbation $\Delta\hat{A}$. Such perturbation theory takes on two equivalent forms: z-independent and z-dependent. The former expresses the new eigenstates and eigenvalues as a power-series expansion in $\Delta\hat{A}$. The latter expands a propagating state $|\psi\rangle$ in the basis of the *unperturbed* states $|n\rangle$, with z-varying expansion coefficients. Such a z-dependent expansion is often called "coupled-mode theory" in electromagnetism [23, 45].

The main results from the z-independent theory that we will employ here are that the first- and second-order corrections to an eigenvalue β_n are given by:

$$\Delta\beta_n^{(1)} = \left\langle n \middle| \Delta\hat{A} \middle| n \right\rangle, \tag{43}$$

$$\Delta\beta_n^{(2)} = \sum_{n'\neq n} \frac{\left| \left\langle n' \middle| \Delta\hat{A} \middle| n \right\rangle \right|^2}{\Delta\beta_{nn'}}, \tag{44}$$

where $\Delta\beta_{nn'} \equiv \beta_n - \beta_{n'}$. Because of the smallness of the perturbations we consider, we generally only use the second-order correction if the first-order correction is zero by some symmetry. A minor modification must be made in the case of degenerate (equal-β) modes, such as $\pm m$ pairs in cylindrical fibers; in this case, the degeneracy is typically broken by $\Delta\hat{A}$, and the first-order splitting is given by diagonalizing the $\Delta\hat{A}$ operator in the basis of the degenerate modes.

In z-dependent perturbation theory, a state $|\psi\rangle$ in the perturbed waveguide is expanded in the unperturbed eigenstates $|n\rangle$ with coefficients $c_n(z)$, satisfying:

$$\frac{dc_n}{dz} = i\beta_n c_n + i \sum_{n'} \left\langle n \middle| \Delta\hat{A} \middle| n' \right\rangle c_{n'}. \tag{45}$$

These equations are exact if all modes are included in the expansion. In the most common case, one starts with only one mode $c_n(0) = 1$ and wishes to find the lost power $|c_{n'}(z)|^2$ in "parasitic" (scattered) modes $|n'\rangle$ after some distance z. Eq. (45) can be approximately solved in that case to lowest-order for a *uniform* perturbation $\Delta\hat{A}$, yielding:

$$\frac{|c_{n'}(z)|^2}{|c_n(0)|^2} \cong \frac{4 \left| \left\langle n' \middle| \Delta\hat{A} \middle| n \right\rangle \right|^2}{\Delta\beta_{n'n}^2} \sin^2\left(\Delta\beta_{n'n} z/2\right). \tag{46}$$

Thus, the lost power oscillates rather than growing steadily—this is due to destructive interference in the scattering, as long as $\Delta\beta \neq 0$. This fortunate interference is stymied, however, if the modes are lossy or if $\Delta\hat{A}$ contains some non-uniform disorder, a fact that we considered with Eq. (16) and in Sec. 8.3.

For perturbations that vary smoothly in z, one can alternatively expand in the instantaneous eigenstates $|n(z)\rangle$ and $\beta_n(z)$ of $\hat{A}(z)$, in which case the coefficients obey:

$$\frac{dc_n}{dz} = i\beta_n c_n - \sum_{n'\neq n} \frac{\left\langle n \middle| \frac{d\hat{A}}{dz} \middle| n' \right\rangle}{\Delta\beta_{n'n}} c_{n'}. \tag{47}$$

One can see, qualitatively, that changes slow compared to the lengthscale of $1/\Delta\beta$ should cause small scattering and induce adiabatic evolution of the modes; this is proved rigorously in [52].[17]

---

[17]This adiabaticity was also considered in [53], where it was erroneously claimed that an analogue of Eq. (41) could be expressed as an ordinary (non-generalized) Hermitian eigenproblem with the same field-state representation (leading to an incorrect orthogonality relation).

Although both Eq. (44) and Eq. (46) in principle require an infinity of modes to be included, the $\Delta\beta$ in the denominators implies that one usually need only consider a few modes with nearby β. This is especially true in the case of large-core OmniGuide fibers, in which the close β spacing of the guided modes causes a few couplings to dominate, whereas the cladding (Bragg mirror) modes are at distant β. As a rule of thumb, if a perturbation has a characteristic lengthscale L (*e.g.* the bend radius R_b), only modes with $\Delta\beta \lesssim 1/L$ contribute significantly.

Weak Dielectric Perturbations

One of the most general and important forms of waveguide pertubation is when the dielectric function ε is changed by a small $\Delta\varepsilon$. In this case, we simply compute $\Delta\hat{A}$ by substituting $\varepsilon + \Delta\varepsilon$ into Eq. (38) and subtracting the unperturbed $\hat{A}$. The resulting expression is inconvenient to evaluate directly because it contains derivatives. Since perturbation theory only employs $\Delta\hat{A}$ inside inner products $\langle n'|\Delta\hat{A}|n\rangle$, however, we derive a simpler formulation by integrating by parts and then returning to the six-component field-representation via Eqs. (33–34). This yields:

$$
\left\langle n' \left| \Delta\hat{A} \right| n \right\rangle = \left\langle \begin{array}{c} E'_x \\ E'_y \\ E'_z \end{array} \right| \frac{\omega}{c} \left(\begin{array}{ccc} \Delta\varepsilon & & \\ & \Delta\varepsilon & \\ & & \Delta\varepsilon \end{array} \right) \left| \begin{array}{c} E_x \\ E_y \\ E_z \end{array} \right\rangle + O(\Delta\varepsilon^2). \qquad (48)
$$

Here, we have intentionally dropped terms of $O(\Delta\varepsilon^2)$ or less, even though our general approach ostensibly lacks that limitation (perturbation theory should remain valid as long as $\Delta\varepsilon$ yields a small integral $\langle n'|\Delta\hat{A}|n\rangle$). The reason for this, as we discussed in Sec. 8.2, is that for large $\Delta\varepsilon$ the changing boundary conditions on the fields cause the naïve $\Delta\hat{A}$ to be incorrect. This small-$\Delta\varepsilon$ formula is sufficient to compute absorption losses and nonlinearities, but not for ellipticity or other moving-boundary problems in systems with large index contrasts.

Eq. (48), in conjunction with the first-order shift $\Delta\beta_n^{(1)} = \langle n|\Delta\hat{A}|n\rangle / \langle n|\hat{B}|n\rangle$, has been derived elsewhere by various methods [23, 35, 45]. However, with the exception of [39], it has not been recognized that this expression needs to be corrected for large $\Delta\varepsilon$; we further investigate this limitation in [44].